J. Fluid Mech. (1998), *vol.* 362, *pp.* 121–155. Printed in the United Kingdom

A low-dimensional approach for the minimal flow unit

By BÉRENGÈRE PODVIN AND JOHN LUMLEY

Sibley School of Mechanical and Aerospace Engineering, Cornell University,
Ithaca, NY 14853, USA

(Received 30 October 1996 and in revised form 5 January 1998)

The proper orthogonal decomposition (POD) is applied to the minimal flow unit (MFU) of a turbulent channel flow. Our purpose is to establish a numerical validation of low-dimensional models based on the POD. The simplest (two-mode) model possible is built for the simplified flow in the minimal unit. The dynamical behaviour predicted by the model is compared with that actually occurring in the direct numerical simulation of the flow. The various modelling assumptions which underlie the construction of low-dimensional models are examined and confronted with numerical evidence. The relationship between intermittency in the MFU and intermittent low-dimensional parameters is investigated closely. The agreement observed is quite satisfactory, especially given the crudeness of the truncation considered. To further demonstrate the adequacy of the model, we develop a dynamical filtering procedure to recover information from realistic (partial) measurements. The success obtained illustrates the versatility of the low-dimensional paradigm.

1. Introduction

Over the last thirty years, experimental observers and theoreticians have put together a convincing description of the wall layer. The presence of organized motions or coherent structures is universally agreed upon (see Robinson (1991) for a recent review). In the wall region, coherent structures consist of alternating low- and high-speed streaks combined with a streamwise vortex motion, so that low-speed fluid is violently lifted up from the wall, while high-speed fluid is gently pushed down towards it. Some researchers also report observing 'hairpin' vortices, the legs of which are very similar to streamwise rolls. Kline *et al.* (1967) and Corino & Brodkey (1969) were among the first to observe the recurring formation and breakdown of these structures. Such regeneration cycles were termed 'bursting events'. Kim, Kline & Reynolds (1971) found a connection between the occurrence of these bursts and the production of turbulence. Considerable effort has been made in recent years to understand the dynamics of the process. However, progress in that area has been relatively slow. The fundamental reason for this is probably the closure problem or how to bring the turbulent phenomenon down to a finite number of parameters. Some of the difficulties may be solved by adequate modelling. More importantly, the success of an analysis will rely heavily upon the availability of powerful, objective, relevant extraction tools.

The proper orthogonal decomposition (POD) first introduced in turbulence by Lumley (1967) is such a tool. In this decomposition, the spatio–temporal velocity field is represented as the superposition of an infinity of spatial (coherent) structures whose amplitude varies in time. The POD has been applied with a considerable success to a wide variety of domains, ranging from free shear flows (Sirovich, Kirby & Winter 1990) to flames (Torniainen, Hinz & Gouldin 1997). It was first applied by Bakewell & Lumley (1967) for an experimental turbulent channel flow. Moin & Moser (1989) later applied it to a numerical turbulent channel flow. In both cases the procedure led to the identification of a characteristic eddy consisting of a pair of counter-rotating streamwise vortices, which produce a strong updraught of low-momentum fluid into the core region and a more gentle downdraught of high-speed fluid towards the wall. The centre of the vortices is about 30 wall units (based on the wall friction velocity and fluid viscosity) from the wall. The typical spanwise width of the structure is around 100 wall units. Their length in the streamwise direction is known with less precision. It is observed to increase with the distance from the wall and ranges between values of 400 and 1000 wall units (Hinze 1976).

Aubry *et al.* (1988) used the POD to derive low-dimensional models from the Navier–Stokes equations. Their goal was to obtain evolution equations for the amplitude of the coherent structures which capture in some sense the bursting process. They produced a very low-order system which exhibited intermittent features reminiscent of those found in experimental flows. By intermittent we mean that the system alternated between long periods of relative quiescence and short periods of high excitation. Zhou & Sirovich (1992) also obtained dynamical systems from the same method, which they call the Karhunen–Loeve decomposition.

The potential represented by low-dimensional models extends over a wide range of applications, among which turbulence control occupies a prominent position. Steps have already been made in this direction. Coller, Holmes & Lumley (1994) developed a strategy based on low-dimensional models to control the bursting of vortices using adjacent vortex pairs created by a wall actuator. Beyond direct application to real flows, the long-term goal of this type of approach is the development of a methodology for efficient, ‘smart’ control.

Alternatively, flow simplification can be achieved numerically by decreasing the physical extent of the domain so as to keep only a few (or even one) coherent structures. Jimenez & Moin (1991) found that turbulence could not be sustained in computational boxes below a certain size, which they called a minimal flow unit (MFU). They identified a critical spanwise dimension of 100 wall units which corresponds to the typical streak spacing observed in experiments. The minimal flow unit presents some strongly turbulent features, yet the flow dynamics are simplified and the computational expense significantly less than for a full flow simulation. As such, it has proven a very useful frame in which to study the dynamics of coherent structures: see for instance Hamilton, Kim & Waleffe (1995). The minimal flow unit is also an ideal testbed for control strategies. Carlson & Lumley (1996) examined the effect of raising a moving wall in the minimal flow unit of a turbulent channel flow.

The strength of low-dimensional models lies largely in their considerable flow reduction power, but this strength may become a weakness if they are not carefully appraised and interpreted. This work constitutes a first step in this direction. In this paper, we use the minimal flow unit to check both assumptions and predictions made with POD-based low-dimensional models. The idea seems all the more appropriate as the physical domain spanned by low-dimensional models shrinks to the minimal flow unit when the minimum number of POD modes is retained. The first step is to apply the POD to the minimal flow unit. Comparing the coherent structures thus extracted to those of a truly turbulent flow constitutes an extra validation of the simplified flow calculation. Next, the simplest low-dimensional model possible (two-mode) is constructed for the simplified flow using adequate assumptions. Its properties have been studied mathematically elsewhere by Armbruster, Guckenheimer & Holmes (1988). Then the POD modes as well as the different contributions to the model evolution equations are computed directly from the simulation and compared with the model. We emphasize the relationship between POD (mathematical) quantities and standard (physical) bursting indicators. Despite the model limitations, this study should help set general evaluation criteria for low-dimensional models, and also give us a better insight in the flow dynamics.

This paper is organized as follows: in §2, we apply the POD decomposition to the MFU. In §3, we present the modelling assumptions that underlie the derivation of low-dimensional models. In §4, we focus on the two-mode model. We compare theoretical results to the numerically computed histories of the POD coefficients. In §5, we provide a quantitative appraisal of the modelling assumptions. In §6, we try to relate the dynamical behaviour predicted by our model to objective features of the minimal flow unit. In particular, we characterize the intermittency cycle first observed by Jimenez & Moin (1991) with low-dimensional estimates. In §7, we propose a potential application for our approach: we design an estimation procedure based on the model to solve a realistic information problem. We present our conclusions in §8.

2. The proper orthogonal decomposition (POD) in the MFU

2.1. *The POD*

We first give a succint description of the POD. We only mention here what is indispensable to the comprehension of this paper. For more details the reader is referred to Aubry (1987), Herzog (1986), Berkooz (1991), Aubry *et al.* (1988) and Berkooz, Holmes & Lumley (1993*b*). In the case of a fully developed turbulent channel flow – which means in particular homogeneity in the streamwise (x) and spanwise (z) directions and quasi-stationarity – the velocity field $\tilde{\boldsymbol{u}}(x,y,z,t)$ can be decomposed into a mean part $\boldsymbol{U}(y,t)$ (the average is performed over horizontal planes $y=C$, where C is a constant) and a fluctuating part $\boldsymbol{u}(x,y,z,t)$.

$$\tilde{\boldsymbol{u}}(x,y,z,t)=\boldsymbol{U}(y,t)+\boldsymbol{u}(x,y,z,t). \tag{1}$$

The Karhunen–Loève theorem states that there exists an infinite set of eigenfunctions and eigenvalues $(\boldsymbol{\phi}^n,\lambda^n)$ such that

$$\boldsymbol{u}(x,y,z,t)=\sum_n a^n(t)\boldsymbol{\phi}^n(x,y,z),$$

where a^n are uncorrelated random coefficients of variance λ^n. These eigenmodes correspond to the structures which are the best correlated with the fluctuating velocity field. In homogeneous directions, POD eigenmodes are simply Fourier modes. In the wall-normal direction and in Fourier space, the eigenfunctions $\boldsymbol{\phi}^n$ associated with the eigenvalue λ^n are solutions of

$$\int\langle\hat{u}^i_{\boldsymbol{k}}(y)\hat{u}^{*j}_{\boldsymbol{k}}(y')\rangle\phi^{nj}_{\boldsymbol{k}}(y')\,\mathrm{d}y'=\lambda^n_{\boldsymbol{k}}\phi^{ni}_{\boldsymbol{k}}(y), \tag{2}$$

where $\langle\,\rangle$ denotes an ensemble average, $\hat{\boldsymbol{u}}_{\boldsymbol{k}}(y,t)$ represents the Fourier transform of the velocity field in the horizontal directions and $\langle\hat{u}^i_{\boldsymbol{k}}(y)\hat{u}^{*j}_{\boldsymbol{k}}(y')\rangle$ is the Fourier transform in the homogeneous directions of the spatial autocorrelation tensor at zero time lag $R^{ij}(x,y,z,x',y',z')=\langle u^i(x,y,z,t)u^j(x',y',z',t)\rangle$.

Let $\boldsymbol{k} = (k_1, k_3)$. The velocity field is then decomposed as follows:

$$\hat{\boldsymbol{u}}_{k_1,k_3}(y,t) = \sum_{k_1,k_3,n} a^n_{k_1,k_3}(t)\boldsymbol{\phi}^n_{k_1,k_3}(y)$$

We choose to normalize the eigenfunctions such that

$$\int_{domain} \phi^{ni}_{k_1,k_3}(y)\phi^{*ni}_{k_1,k_3}(y)\,\mathrm{d}y = 1$$

so that

$$\langle a^n_{k_1,k_3}(t) a^{*n}_{k_1,k_3}(t)\rangle = \lambda^n_{k_1,k_3}.$$

This decomposition is optimal in the sense that it captures the maximum energy. The first n POD eigenfunctions capture more energy on average than any other decomposing set of n elements. From now on we will identify coherent structures with the structures built from POD eigenfunctions. We point out that this choice may not exactly correspond to traditional definitions of coherent structures. Assuming zero phase lag between consecutive wavenumbers, the first structure ($n = 1$) for the wall layer turns out to represent a pair of counter-rotating streamwise vortices producing a strong updraught of low-momentum fluid between them. The first structure and the first three structures respectively account for 60 % and 90 % of the total kinetic energy of the wall region. More than 100 % of the shear stress is captured by the first eigenfunction, which means that higher-order eigenfunctions make negative contributions to the shear stress.

We now introduce some notation that will be of use in the next sections. In practice, we consider a finite set of POD modes. Let

$$T(l,m,n) = \{a^p_{\boldsymbol{k}} \mid |k_1| \leqslant l, |k_3| \leqslant m, p \leqslant n\} \tag{3}$$

so that we can write

$$u^i = u^i_< + u^i_>, \tag{4}$$

where $u^i_<$ represents the projection on the space spanned by $T(l,m,n)$ and $u^i_>$ represents the complement of that projection into the unresolved space.

2.2. *The minimal flow unit* (*MFU*)

The code used for the numerical simulation is the one described in Carlson (1995) for a turbulent channel flow with no-slip walls. It is a pseudo-spectral code with Fourier modes in the streamwise and spanwise directions denoted respectively x and z, and Chebyshev polynomials in the normal direction y. The directions x, y, z may at times be called x_1, x_2, x_3. Similarly, their respective velocity components u, v, w may be referred to as u^1, u^2, u^3.

Velocity is advanced in time in the equations through a third-order Runge–Kutta method. Constant mass flux was imposed, which means that the mean pressure gradient varied in time. Boundary conditions for the pressure were solved via a matrix influence technique.

The Reynolds number chosen based on the channel half-height and centreline velocity was $R = 4000$. The box dimensions were $(L_1, L_2, L_3) = (2\pi/3, 2, \pi/3)$. The variables in the code used to non-dimensionalize were the channel half-height h and the outer velocity U (centreline velocity of a laminar parabolic profile with the same volume flux). Wall units based on the average friction velocity u_* and the viscosity ν will be denoted by a $+$. The number of modes employed was $(N_1, N_2, N_3) = (32, 65, 16)$.

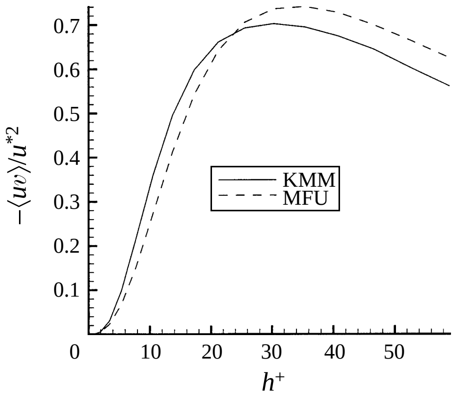

FIGURE 1. Reynolds Stresses in the wall layer for the MFU and the full flow simulation (Kim, Moin & Moser (KMM) data kindly provided by R. Moser).

Careful examination of the spectra showed that the flow was adequately resolved. The Reynolds number based on the average friction velocity u_* and channel half-height was about 180, which is the same as in Moin & Moser's calculation. The flow consists of a doubly infinite array of structures, each structure being the same pair of low-/high-speed streaks. Statistics for the inner region are comparable to those of a fully turbulent flow. See figure 1 or Carlson & Lumley (1996) for a complete examination of the turbulence statistics. The agreement is less satisfactory for the outer region Jimenez & Moin (1991). Hopefully this discrepancy should not affect our results too much, the focus of our study being the wall layer.

2.3. *The POD in the minimal flow unit*

In this paragraph we solve equation (2). Our procedure is very similar to Moin & Moser's (1989) who applied the POD to the simulation of a fully developed turbulent channel flow.

To compute the kernel, i.e the Fourier transform of the autocorrelation tensor,

$$\Phi_{\boldsymbol{k}}^{ij}(y,y') = \langle \hat{u}_{\boldsymbol{k}}^{i}(y)\hat{u}_{\boldsymbol{k}}^{*j}(y')\rangle \tag{5}$$

we used an ensemble average over velocity fields taken at sufficiently large time intervals to be uncorrelated. We quadrupled our initial number of samples by making use of the kernel symmetries

$$\Phi_{\boldsymbol{k}}^{ij}(y,y') = \Phi_{\boldsymbol{k}}^{ij}(y',y),$$
$$\Phi_{k_1k_3}^{ij}(y,y') = \omega_{ij}\Phi_{k_1-k_3}^{ij}(y,y'),$$

where

$$\omega_{ij} = \begin{cases} 1 & \text{if } i \text{ or } j \text{ are both equal to or both different from 3} \\ -1 & \text{otherwise.} \end{cases}$$

Like Moin & Moser, we used the trapezoidal rule as our method of integration, which allowed some flexibility in the choice of the domain of decomposition. Since the characteristics of wall layers are assumed to be universal when normalized with wall units, and our channel half-height is the same in wall units as Moin & Moser's (180+), we chose to compare the full half-channel lowest-order eigenfunctions and

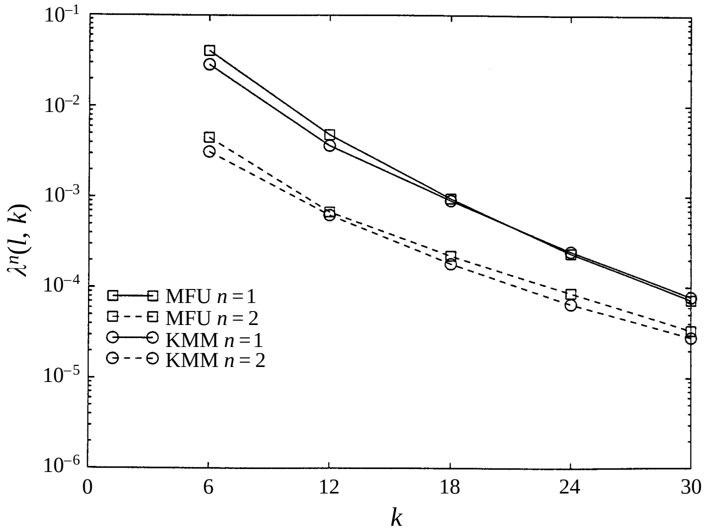

FIGURE 2. Eigenvalue spectrum for the zero streamwise wavenumber.

eigenvalues. To derive our low-dimensional model, we perform the decomposition on the wall layer, i.e. the region $0 \leqslant y \leqslant 40+$. This corresponds to the extent of the domain chosen by Aubry *et al.* (1988). Note that they used experimental empirical eigenfunctions for the wall layer Herzog (1986).

Figure 2 compares our eigenvalue spectrum for the first two eigenmodes $\lambda_k^{n=1,2}$ at zero streamwise wavenumber with Moin & Moser's full flow computation. Overall there is very little difference between the two spectra. The discrepancy in the spectra, as could be expected, is largest for the first wavenumber, and decreases rapidly with the smaller scales which are less sensitive to the difference in size of the computational box. Figure 3 compares the dominant eigenfunction of the MFU and Moin & Moser's eigenfunction corresponding to the same wavelength in wall units (about 185+). The close agreement shows that the first coherent structures of the MFU do corrrespond to what would be found in a real wall layer. It also justifies *a posteriori* our mixing two different (ensemble and spatial) averages.

We plan to carry out a more detailed comparison of the higher-order structures in the near future. We note that Webber, Handler & Sirovich (1997) recently found that in the minimal flow unit fewer modes were needed to capture a given amount of energy than in a full channel flow, which again reflects the structural simplicity of the minimal flow unit. This point being made, we now examine the building principles of low-dimensional models.

3. Deriving a low-dimensional model

In this section we make explicit the relationship between the Navier–Stokes equations and the system of ODEs which constitute the low-dimensional models. It is not our purpose here to give a lengthy derivation of the low-dimensional model. We refer the reader for this to Aubry (1987), Aubry *et al.* (1988), Berkooz (1991). Our main goal is to give a clear account of the different modelling assumptions embodied in the model, which will later be confronted with the numerical simulation of the minimal flow unit.

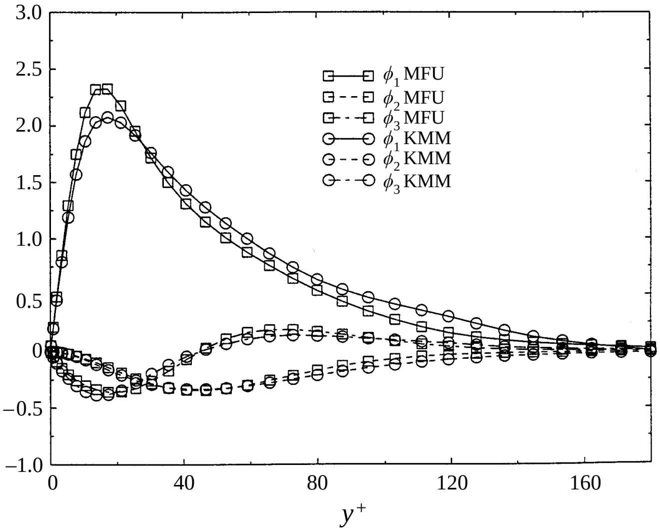

FIGURE 3. Eigenfunction for the dominant mode $a^1_{0,1}$.

We briefly outline how the model equations are obtained. Starting from the Navier–Stokes equation for an incompressible fluid

$$\frac{\partial \tilde{u}^i}{\partial t} = -\tilde{u}^j \frac{\partial \tilde{u}^i}{\partial x_j} - \frac{1}{\rho}\frac{\partial \tilde{p}}{\partial x_i} + \nu \frac{\partial \tilde{u}^i}{\partial x_k x_k} \tag{6}$$

and introducing the decomposition (1) into them, we obtain

$$\frac{\partial u^i}{\partial t} = -u^j \frac{\partial u^i}{\partial x_j} - U^j \frac{\partial u^i}{\partial x_j} - u^j \frac{\partial U^i}{\partial x_j} - \frac{1}{\rho}\frac{\partial p}{\partial x_i} + \nu \frac{\partial u^i}{\partial x_k x_k}. \tag{N^i}$$

To obtain an evolution equation for the mode $a^n_{\boldsymbol{k}}$, we project N^i onto the corresponding eigenfunction, that is we take its Fourier transform $N^i_{\boldsymbol{k}}$ then compute the inner product $\int_{domain} N^i_{\boldsymbol{k}} \phi^{*ni}_{\boldsymbol{k}}$. For any finite truncation of POD modes $T(l, m, n)$, the set of ODEs obtained is not in closed form. Modelling assumptions are required in order to close the system. We focus on the assumptions and check them in detail in §5. The system of ODEs is then derived term-to-term from the Navier–Stokes equations.

3.1. *The mean velocity profile*

We first need a correct expression for the mean shear, where 'mean' here refers to a horizontal spatial average which we will denote from now on by $\langle\,\rangle$. The mean velocity profile $\langle \tilde{u} \rangle = U(y, t)$ is a function of the vertical position, and also varies in time. The mean shear constitutes the main source of energy for the turbulence. It represents a finite supply, so that its intensity will be affected by what the large scales have extracted from it (in other words a feedback term should appear in its expression). The derivation of the expression will not be reproduced here and can be found in Aubry *et al.* (1988). From the equation for the mean velocity profile $\boldsymbol{U} = U(y, t)\boldsymbol{e}_2$

$$\frac{\partial U}{\partial t} = -\frac{\partial \langle uv \rangle}{\partial y} - \frac{1}{\rho}\frac{\partial p}{\partial y} + \nu \frac{\partial U}{\partial y^2} \tag{7}$$

we obtain the following model:

$$U(y,t)=\frac{u_*^2(t)}{\nu}\left(y-\frac{y^2}{2h}\right)+\frac{1}{\nu}\int_0^y\langle uv\rangle(y',t)\,\mathrm{d}y. \tag{8}$$

The expression is exact if the mean velocity field is stationary. Berkooz, Holmes & Lumley (1993) showed that provided that the box dimensions are sufficiently large, the temporal variations of the mean velocity field can be expected to be slow compared to the time scale of the model.

To put the expression in closed form, we represent $\langle uv\rangle$ by its projection on the space spanned by the truncation $T(l,m,n)$. This gives cubic terms which are all strictly negative in the case where only one eigenfunction is considered.

3.2. *The small-scale stress tensor*

At the other end of the spectrum, energy is transferred from the larger resolved to the smaller unresolved scales, which defines a cascade process. In practice, we usually consider severely restricted truncations so that we need to provide some mechanism by which energy from the large scales may be dissipated. Since large scales are likely to be unaffected by the detail of the small-scale behaviour, this mechanism does not need to be particularly accurate. A simple eddy viscosity transport model or Heisenberg model was therefore employed.

We make the following decomposition:

$$u^iu^j=u^i_<u^j_<+[u^i_>u^j_<+u^i_<u^j_>+u^i_>u^j_>]. \tag{9}$$

The second and third terms are called Leonard stresses. They represent cross-interactions between resolved and unresolved modes. They have been found to be relatively unimportant (Holmes, Lumley & Berkooz 1996) and were neglected in Aubry's derivation. We chose to include them in the expression for the small-scale stress tensor. Let

$$-\tilde{\tau}_{ij}=u^iu^j-u^i_<u^j_<.$$

We define

$$\tau_{ij>}=\langle\tilde{\tau}_{ij}\rangle_>-\langle\langle\tilde{\tau}_{ij}\rangle_>\rangle-\tfrac{1}{3}\delta_{ij}(\langle\tilde{\tau}_{kk>}\rangle_>-\langle\langle\tilde{\tau}_{kk}\rangle_>\rangle), \tag{10}$$

where $\langle\,\rangle_>$ is an operator averaging over the unresolved scales and δ_{ij} is the Kronecker delta. The eddy viscosity or Heisenberg model stipulates that the anisotropic small-scale stress tensor must be proportional to the strain rate of the resolved scales $s_{ij<}$:

$$\tau_{ij>}=2\tilde{\nu}_Ts_{ij<}=\tilde{\nu}_T(u^i_{<,j}+u^j_{<,i}), \tag{11}$$

where the commas stand for differentiation. Let

$$\tilde{\nu}_T=\alpha\nu_T=\alpha u_>l_>,$$

where $u_>$ and $l_>$ are respectively velocity and length scales characteristic of the unresolved modes, and α is a non-dimensional parameter $O(1)$ which characterizes the amount of energy being dissipated. Throughout the paper α will be called the Heisenberg parameter and it is expected to vary in a real flow: different values of α may correspond to different dynamical behaviours. We used the same value for ν_T as Aubry *et al.* (1988), i.e. $\nu_T=6.28$.

The Navier–Stokes equations become

$$\frac{\partial u^i_<}{\partial t}=-u^j_<\frac{\partial u^i_<}{\partial x_j}-U^j\frac{\partial u^i_<}{\partial x_j}-u^j_<\frac{\partial U^i}{\partial x_j}-\frac{1}{\rho}\frac{\partial}{\partial x_i}(p+\tfrac{1}{3}\langle u^k_>u^k_>\rangle_>)+(\nu+\alpha\nu_T)\frac{\partial u^i_<}{\partial x_kx_k} \tag{$N^i_<$}$$

3.3. *Higher-order wall-normal eigenmodes*

We now consider the POD higher modes $a_{\boldsymbol{k}}^p \in H(l,m,n)$ where

$$H(l,m,n) = \{a_{\boldsymbol{k}}^p \| k_1| \leqslant l, |k_3| \leqslant m, p > n\}.$$

These modes arise in the equations through the mean shear–fluctuation and the fluctuation–fluctuation interactions. Owing to the huge energy gap between consecutive eigenmodes, they were neglected by Aubry *et al.* In §5, we will compute the effect of the interaction of these higher-order modes with the mean velocity profile. For the fluctuation–fluctuation interaction, we will compute globally the quadratic contribution from the low Fourier modes, i.e. the modes in $H(l,m,n)$ and those in $T(l,m,n)$. We do not include the higher-order eigenmodes in the expression of the small-scale tensor containing high Fourier modes. The main reason for doing that is consistency with other approaches not based on the POD such as Hamilton *et al.* (1995), where small scales conventionally refer to high Fourier modes.

3.4. *General derivation*

We start from the Navier–Stokes equations

$$\frac{\partial u^i}{\partial t} = -u^j\frac{\partial u^i}{\partial x_j} - U^j\frac{\partial u^i}{\partial x_j} - u^j\frac{\partial U^i}{\partial x_j} - \frac{1}{\rho}\frac{\partial p}{\partial x_i} + \nu\frac{\partial u^i}{\partial x_k x_k}. \qquad (N(i))$$

Let $\boldsymbol{k} = (l,k)$. To obtain the evolution equation for the mode $a_{\boldsymbol{k}}^n$, we compute $\int N_{\boldsymbol{k}}^i \phi_{\boldsymbol{k}}^{i*n}$:

$\partial u^i/\partial t$ becomes $\dot{a}_{\boldsymbol{k}}^n$;

$-u^j\partial U^i/\partial x_j$ yields

linear terms $br_{\boldsymbol{k}}^{1mn} a_{\boldsymbol{k}}^m$, where

$$br_{\boldsymbol{k}}^{1mn} = \int \frac{u_*^2}{\nu}(1 - y/h)\phi_{\boldsymbol{k}}^{2m}\phi_{\boldsymbol{k}}^{*1n}\,\mathrm{d}y$$

and cubic terms $dr_{\boldsymbol{k}\boldsymbol{k}'}^{pqrn} a_{\boldsymbol{k}'}^p a_{\boldsymbol{k}'}^{*q} a_{\boldsymbol{k}}^r$, where

$$dr_{\boldsymbol{k}\boldsymbol{k}'}^{pqrn} = \frac{1}{\nu}\int \phi_{\boldsymbol{k}'}^{*2q}\phi_{\boldsymbol{k}'}^{1p}\phi_{\boldsymbol{k}}^{2r}\phi_{\boldsymbol{k}}^{*1n}\,\mathrm{d}y;$$

$-U^j\partial u^i/\partial x_j$ yields

linear terms $bi_{\boldsymbol{k}}^{1mn} a_{\boldsymbol{k}}^m$, where

$$bi_{\boldsymbol{k}}^{1mn} = -\mathrm{i}l\int \frac{u_*^2}{\nu}\frac{y}{h}\phi_{\boldsymbol{k}}^{im}\phi_{\boldsymbol{k}}^{*in}\,\mathrm{d}y$$

and cubic terms $di_{\boldsymbol{k}\boldsymbol{k}'}^{pqrn} a_{\boldsymbol{k}'}^p a_{\boldsymbol{k}'}^{*q} a_{\boldsymbol{k}}^r$, where

$$di_{\boldsymbol{k}\boldsymbol{k}'}^{pqrn} = -\frac{\mathrm{i}l}{\nu}\int_0^{40+}\left(\phi_{\boldsymbol{k}}^{*in}\phi_{\boldsymbol{k}}^{ir}\int_0^y \phi_{\boldsymbol{k}'}^{*2q}\phi_{\boldsymbol{k}'}^{1p}\,\mathrm{d}y'\right)\mathrm{d}y,$$

where $\mathrm{i} = \sqrt{-1}$. Define

$$b_{\boldsymbol{k}}^1 = br_{\boldsymbol{k}}^1 + bi_{\boldsymbol{k}}^1, \quad d_{\boldsymbol{k}\boldsymbol{k}'} = dr_{\boldsymbol{k}\boldsymbol{k}'} + di_{\boldsymbol{k}\boldsymbol{k}'}$$

In the case where $l = 0$, $bi_{\boldsymbol{k}}^1 = di_{\boldsymbol{k}\boldsymbol{k}'} = 0$. Also, in the case when one eigenfunction only is considered, which is the case for our two-mode model, all the coefficients $d_{\boldsymbol{k}\boldsymbol{k}'}$ are negative. One can then show that the system is globally stable. The source term $br_{\boldsymbol{k}}^1$ represents the energy supply provided by the mean shear.

Denote

$$\Omega^j = \begin{cases} \mathrm{i}k_j & \text{if } j = 1 \text{ or } j = 3 \\ \mathrm{d}/\mathrm{d}y & \text{if } j = 2. \end{cases}$$

Then $\nu \partial u^i / \partial x_k x_k$ yields linear terms $-b_{\boldsymbol{k}}^{2mn} a_{\boldsymbol{k}}^m$, where

$$-b_{\boldsymbol{k}}^{2mn} = \int \nu (\Omega^j)^2 \phi_{\boldsymbol{k}}^{im} \phi_{\boldsymbol{k}}^{*in} \, \mathrm{d}y.$$

As expected, $b_{\boldsymbol{k}}^{2mn}$ is in general positive. Its magnitude was found to be very small compared to the other terms in the equation and we therefore chose to neglect such terms.

$-u^j \partial u^i / \partial x_j$ is decomposed into a resolved and an unresolved part.

The resolved part gives quadratic terms $c_{\boldsymbol{k}'\boldsymbol{k}-\boldsymbol{k}'}^{pqn} a_{\boldsymbol{k}'}^p a_{\boldsymbol{k}-\boldsymbol{k}'}^q$ where

$$c_{\boldsymbol{k}'\boldsymbol{k}-\boldsymbol{k}'}^{pqn} = \int \phi_{\boldsymbol{k}'}^{jp} \Omega_{\boldsymbol{k}-\boldsymbol{k}'}^j \phi_{\boldsymbol{k}-\boldsymbol{k}'}^{iq} \phi_{\boldsymbol{k}}^{*in} \, \mathrm{d}y;$$

$c_{\boldsymbol{k}'\boldsymbol{k}-\boldsymbol{k}'}^{pqn}$ can be either negative or positive.

The unresolved part can be decomposed into an anisotropic and isotropic (pseudo-pressure) part. As we have just seen, the anisotropic component of the unresolved part is modelled by a linear term $-\alpha b_{\boldsymbol{k}}^{2n} a_{\boldsymbol{k}}^n$. The Heisenberg parameter α characterizes the amount of energy transfer from the large scales to the small scales. α is taken to be constant in the model. The isotropic component of the unresolved part is also modelled using a Heisenberg-like approximation and yields extra quadratic interactions (see Aubry (1987) for details). The contribution of this pseudo-pressure term was found to be negligible.

$-(1/\rho)(\partial p / \partial x_i)$ yields a term evaluated at the edges of the domain $-[\hat{p}_{\boldsymbol{k}} \phi_{\boldsymbol{k}}^{*2n}]_{y=0}^{y=40+}$. This term represents the influence of the outer layer and behaves like a stochastic forcing term. Its magnitude was found to be very small and it was omitted from the present analysis.

Finally, we obtain a system of equations for $T(l,m,n)$ in closed form such that for $a_{\boldsymbol{k}}^j \in T(l,m,n)$ (the tensor rule does not apply here)

$$\dot{a}_{\boldsymbol{k}}^j = \sum_p \mu_{\boldsymbol{k}}^{pj} a_{\boldsymbol{k}}^p + \sum_{pq} \sum_{\boldsymbol{k}'} c_{\boldsymbol{k}'\boldsymbol{k}-\boldsymbol{k}'}^{pqj} a_{\boldsymbol{k}'}^p a_{\boldsymbol{k}-\boldsymbol{k}'}^q + \sum_{pqr} \sum_{\boldsymbol{k}'} d_{\boldsymbol{k}\boldsymbol{k}'}^{pqrj} a_{\boldsymbol{k}'}^p a_{\boldsymbol{k}'}^{*q} a_{\boldsymbol{k}}^r, \tag{12}$$

where

$$\mu_{\boldsymbol{k}}^{pj} = b_{\boldsymbol{k}}^{1pj} - (1 + \alpha \nu_T) b_{\boldsymbol{k}}^{2pj}.$$

4. The two-mode (four-dimensional) model

For the purpose of numerical validation we consider a two-mode model, which is the simplest model originally studied by our group (see Stone (1989)). The physical domain corresponding to that model is a minimal flow unit that contains one low- and one high-speed streak, and at most one pair of counter-rotating vortices. The coefficients of the two-mode model are computed using the empirical eigenfunctions obtained in §1 and the formulae given in §3. The model belongs to the class of four-dimensional systems with SO(2) symmetry, which corresponds in physical space to invariance by horizontal translations and invariance by reflection with respect to a plane parallel to the directions x and z. This family of systems has been studied extensively by Armbruster *et al.* (1988). We first present some of their results. The two-mode model predicts the amplitude of the POD modes present in the truncation. Here we can compare this prediction to the true amplitude computed at each instant by projecting the three-dimensional velocity field in the numerical simulation onto the corresponding eigenfunctions.

In this section we focus on the qualitative aspects of the comparison, i.e. we examine if and how two-mode models can generally reproduce the dynamical behaviour of the POD modes. Quantitative comparison is deferred until §6, once the modelling assumptions and therefore the exact form of the model have been validated in §5.

4.1. *Theoretical results on the two-mode model*

We are interested in $T(0,2,1)$ which represents the first two most energetic modes, that is the first eigenmode of the first two spanwise wavenumbers with no streamwise variations. In that case, the system of ODEs (12) can be written as

$$\left.\begin{aligned} \dot{a}_1 &= \mu_1 a_1 + c_{-1,2} a_1^* a_2 + (d_{11}|a_1|^2 + d_{12}|a_2|^2) a_1, \\ \dot{a}_2 &= \mu_2 a_2 + c_{1,1} a_1^2 + (d_{21}|a_1|^2 + d_{22}|a_2|^2) a_2, \end{aligned}\right\} \tag{13}$$

where $\mu_k = b_{\boldsymbol{k}}^1 - (1 + \alpha \nu_T) b_{\boldsymbol{k}}^2$ and $a_k = a_{0,k}^1$. The bifurcation parameters μ_k represent the balance between the supply from the mean shear and the dissipation to smaller scales.

Let $z_1 = |c_{1,1} c_{-1,2}|^{1/2} a_1$ and $z_2 = |c_{-1,2}| a_2$. Then the equations become

$$\left.\begin{aligned} \dot{z}_1 &= z_1^* z_2 + (\mu_1 + d_{11}|z_1|^2 + d_{12}|z_2|^2) z_1, \\ \dot{z}_2 &= z_1^2 + (\mu_2 + d_{21}|z_1|^2 + d_{22}|z_2|^2) z_2. \end{aligned}\right\} \tag{14}$$

Let $z_j = r_j e^{i\theta_j}$. Due to O(2) symmetry of the equations only the phase difference $\phi = 2\theta_1 - \theta_2$ appears in the equations and the system (14) above can be reduced to

$$\left.\begin{aligned} \dot{r}_1 &= r_1 r_2 \cos\phi + (\mu_1 + e_{11} r_1^2 + e_{12} r_2^2) r_1, \\ \dot{r}_2 &= -r_1^2 \cos\phi + (\mu_2 + e_{21} r_1^2 + e_{22} r_2^2) r_2, \\ \dot{\phi} &= -(2 r_2 - r_1^2/r_2) \sin\phi, \end{aligned}\right\} \tag{15}$$

where $e_{11} = d_{11}/|c_{1,1} c_{-1,2}|$, $e_{12} = d_{12}/|c_{-1,2}|^2$, $e_{21} = d_{11}/|c_{1,1} c_{-1,2}|$ and $e_{22} = d_{22}/|c_{-1,2}|^2$.

In the case when $c_{1,1} c_{-1,2} < 0$, possible equilibrium solutions for this system include fixed points coexisting over a finite domain in (μ_1, μ_2) with travelling waves (see Armbruster *et al.* 1988). We also note the presence of heteroclinic cycles which can easily become unstable for small modifications of the coefficients. As we shall soon see, we are interested in travelling wave equilibria, that is solutions such that $(\dot{r}_1 = 0, \dot{r}_2 = 0, \dot{\phi} = 0)$, but $(\dot{\theta}_1 \neq 0, \dot{\theta}_2 \neq 0)$. Armbruster *et al.* derived a simple analytical expression for them:

$$\left.\begin{aligned} r_2^2 &= -(2\mu_1 + \mu_2)/(4e_{11} + 2e_{12} + 2e_{21} + e_{22}), \\ r_1^2 &= 2 r_2^2, \\ \cos\phi &= \frac{\mu_2(2e_{11} + e_{12}) - \mu_1(2e_{21} + e_{22})}{(-(2\mu_1 + \mu_2)(4e_{11} + 2e_{12} + 2e_{21} + e_{22}))^{1/2}}. \end{aligned}\right\} \tag{16}$$

In physical space, fixed points correspond to a fixed pair of vortices, while travelling waves correspond to a pair of streamwise vortices drifting slowly in the transverse z-direction. Although the wave-like motion is a mathematical representation of the flow behaviour, it does not represent the effect of a wave-inducing physical mechanism such as compressibility. It simply means that sitting at a fixed point in laboratory

(L_1, L_3)	370+	185+
$(b^1_{0,1}, b^1_{0,2})$	0.62	0.65
$(b^2_{0,1}, b^2_{0,2})$	0.042	0.062
$(c_{-1,2}, c_{1,1})$	0.04	−0.20
(d_{11}, d_{12})	−0.336	−0.052
(d_{21}, d_{22})	−0.375	−0.059

Table 1. Coefficients of the dynamical equations in outer variables.

coordinates, a laboratory variable such as the vertical velocity will go up and down as the vortex passes. Due to the width of the box and periodicity conditions, the rolls drift only for a short time before exiting and re-entering the box, which makes the motion periodic. In a real-life situation, in which independent structures interact with each other, and which lacks cross-stream periodicity, the vertical velocity would probably oscillate only once before falling away to zero. Travelling waves bifurcate from the fixed point solution when $|\cos\phi| = 1$.

Table 1 gives the coefficients of the dynamical equations computed in outer variables using the empirical eigenfunctions of the MFU. These coefficients renormalized in wall variables are comparable to those computed in Stone's (1989) study for a box of slightly different dimensions. Due to the strong nonlinearity of the models, small modifications in the coefficients of the equations can significantly alter its dynamics, but the system may also remain almost insensitive to substantial changes in the coefficients. As in Stone's study, we found a parameter range in which unstable heteroclinic cycles coexisted with travelling waves. The bifurcation point for the system between travelling waves and mixed modes ($r_1 \neq 0$, $r_2 \neq 0$) was found to occur for $\alpha = 0.85$ in our system versus $\alpha = 1.32$ in Stone's case.

4.2. *Numerical results*

From the direct numerical simulations (DNS) one obtains the numerical POD mode a^n_k from

$$a^n_k = \int_{domain} \hat{u}^i_k(y)\phi^{ni*}_k(y)\,\mathrm{d}y. \tag{17}$$

From now on, we will omit the suffix when we refer to the first eigenfunction and write a_k for a^1_k.

Time histories of the first two modes are shown in figure 4. Phase portraits are shown in figures 5 and 6. The travelling wave structure of the solution is clearly apparent. The curve labelled TW represents the travelling wave closest in the quadratic sense to the solution computed in the simulation. It does not correspond to the integration of a given system of ODEs, since we do not have a proper criterion to determine the Heisenberg parameter α.

The amplitude of the modes – especially the first mode – was found to be relatively constant, although time fluctuations occur on a typical time scale of $O(100)$ outer units, as figure 16 shows. This time scale was first pointed out by Jimenez & Moin as characterizing some intermittent features of the MFU. The speed of the travelling wave fluctuates over an even longer time scale, $O(500)$. Figure 7 shows the phase difference $\phi = 2\theta_1 - \theta_2 = 2\mathrm{Arg}[a_{0,1}] - \mathrm{Arg}[a_{0,2}]$. This difference oscillates slightly around a constant value, showing that the system is asymptotically – in the phase-average sense – close to an equilibrium state. This phase locking of the modes was

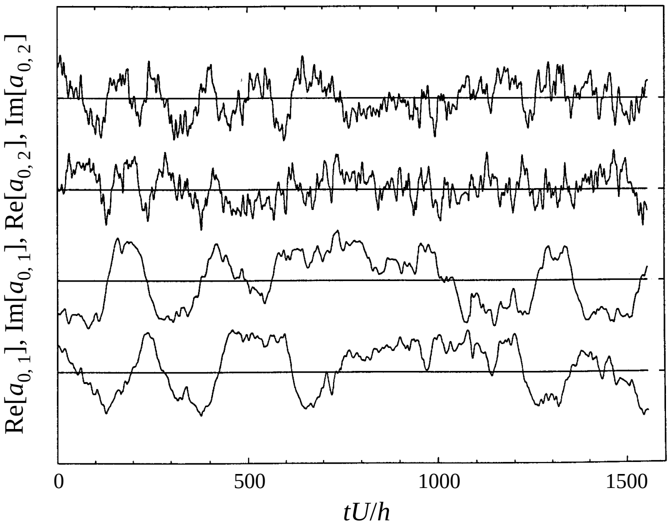

FIGURE 4. Time histories of the POD modes.

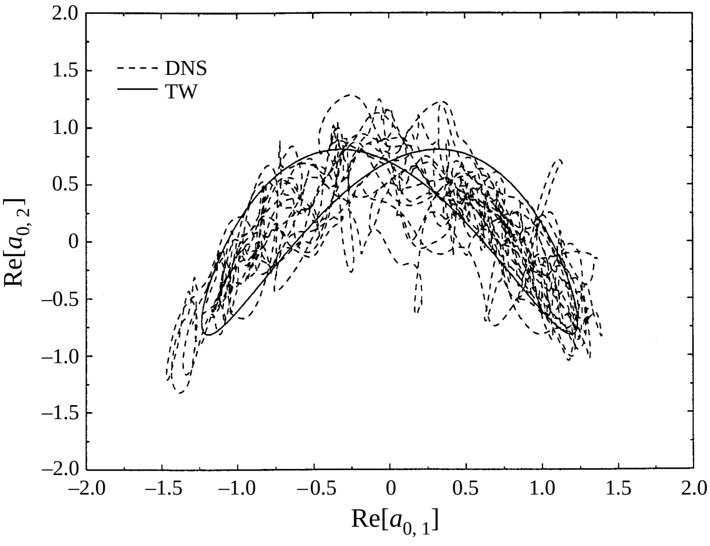

FIGURE 5. Phase portrait for the POD modes (Re[$a_{0,1}$], Re[$a_{0,2}$]).

found to be a persistent feature of our simulation. In some runs (not shown in this paper), we saw it disappear in a few instances as the travelling wave amplitude collapsed abruptly, but such occurrences were rare and extremely brief. The value of the phase locking is very close to π. In phase space, this means that we are very close to the bifurcation point between travelling waves and fixed points. In fact, a closer look at the phase portraits shows that the system alternates between periods of 'fast travel' and 'rest' periods. See for instance in figure 8 how the trajectory slows down in a neighbourhood of the reference time E. Although the two-mode model is not capable of 'bursting' in the same sense as the five-mode model, these intermittent features are reminiscent of the bursting process. We have therefore shown that the

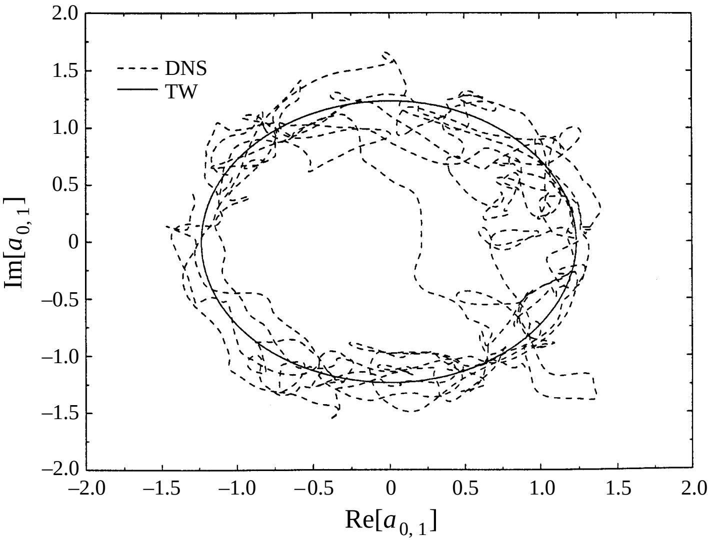

FIGURE 6. Phase portrait for the POD modes ($(\mathrm{Re}[a_{0,1}], \mathrm{Im}[a_{0,1}])$).

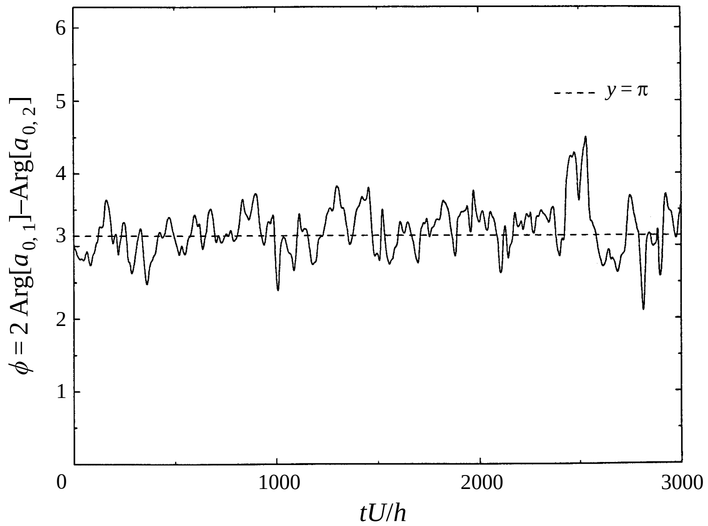

FIGURE 7. Phase difference $\phi = 2\mathrm{Arg}[a_{0,1}] - \mathrm{Arg}[a_{0,2}]$.

two-mode model is able to reproduce qualitatively the large-scale features of the solution, its phase-averaged behaviour as well as its intermittency.

Trajectories in the ten-dimensional model were also an alternation of quiescent periods and violent excursions. However, in the ten-dimensional model, intermittency was observed for a constant value of α, whereas in the four-dimensional model a constant value of α will yield only one type of equilibrium solution. From the point of view of our dynamical system, the change in the dynamical behaviour observed here has to correspond to a change in α. Aubry *et al.* (1988) advanced the idea that the bursting cycle should be associated with an intensification of the energy transfer. Our next step is to compute exactly this energy transfer, i.e. the contribution of the

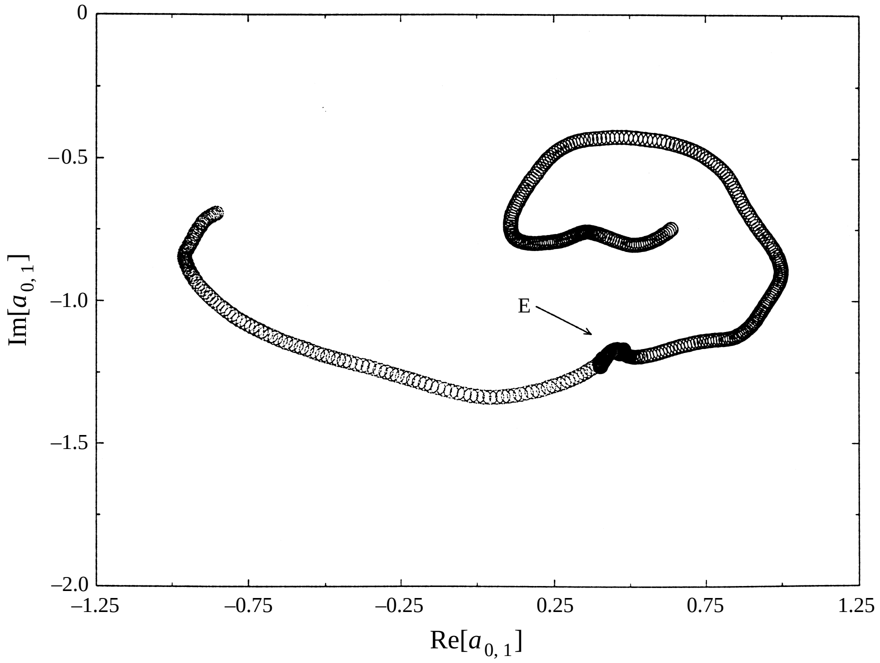

FIGURE 8. Phase portrait for the POD modes – A blow up.

small-scale stress tensor to the large scales, and more generally to confront the main modelling assumptions by numerical evidence. This is the object of the next section.

5. The modelling assumptions

In order to compute intensities and correlation coefficients, we define the scalar product

$$\langle f|g\rangle = \lim_{t\to\infty}\frac{1}{t}\int_0^t fg^*\,\mathrm{d}t \tag{18}$$

and the associated norm

$$\|f\| = \left(\lim_{t\to\infty}\frac{1}{t}\int_0^t |f|^2\,\mathrm{d}t\right)^{1/2}. \tag{19}$$

The correlation coefficient between two generally complex variables a and b is

$$C(a,b) = \frac{Re[\langle a|b\rangle]}{(\langle a|a\rangle\langle b|b\rangle)^{1/2}}. \tag{20}$$

The time average of the quantity a will be denoted $\overline{a}$.

5.1. *The mean velocity profile*

Energy is brought into the streamwise-invariant equations through the term $-v\mathrm{d}U/\mathrm{d}y$ representing advection of the mean shear by the normal turbulent fluctuation. The mean velocity profile is modelled by

$$U(y,t) = \frac{1}{\nu}\int \langle uv\rangle\,\mathrm{d}y + \frac{u_*^2}{\nu}(y - y^2/2h). \tag{21}$$

$\boldsymbol{k} = ((0,1),(0,2))$	DNS	Analytical	Model
$\overline{bd_{\boldsymbol{k}}}$	(0.12, 0.10)	(0.22, 0.20)	(0.03, 0.06)
std$(fd_{\boldsymbol{k}})$	(0.10, 0.11)	(0.12, 0.13)	(0.16, 0.18)

TABLE 2. Mean velocity profile.

In the model $\langle uv\rangle$ is replaced by

$$\langle uv\rangle^M = \sum_{a\in T(0,2,1)} \lambda_{\boldsymbol{k}} |a_{\boldsymbol{k}}|^2 (\phi_{\boldsymbol{k}}^1\phi_{\boldsymbol{k}}^{*2} + \phi_{\boldsymbol{k}}^{*1}\phi_{\boldsymbol{k}}^2). \tag{22}$$

This yields in the dynamical equations a linear term $b_{\boldsymbol{k}}^1 a_{\boldsymbol{k}}$, where

$$b_{\boldsymbol{k}}^1 = \int \frac{u_*^2}{\nu}(1-y/h)\phi_{\boldsymbol{k}}^2\phi_{\boldsymbol{k}}^{*1}\,\mathrm{d}y$$

and cubic terms $d_{\boldsymbol{k}\boldsymbol{k}'}|a_{\boldsymbol{k}'}|^2 a_{\boldsymbol{k}}$, where

$$d_{\boldsymbol{k}\boldsymbol{k}'} = \frac{1}{\nu}\int \phi_{\boldsymbol{k}'}^{*2}\phi_{\boldsymbol{k}'}^1\phi_{\boldsymbol{k}}^2\phi_{\boldsymbol{k}}^{*1}\,\mathrm{d}y.$$

For each mode $(0,k)$, $k = 1,2$, we define

$$\begin{aligned} bd_{\boldsymbol{k}}^{DNS} &= \int \mathrm{d}U/\mathrm{d}y\,\phi_{\boldsymbol{k}}^2\phi_{\boldsymbol{k}}^{*1}, \\ bd_{\boldsymbol{k}}^{analytical} &= b_{\boldsymbol{k}}^1 + \frac{1}{\nu}\int \langle uv\rangle \phi_{\boldsymbol{k}}^{*1}\,\mathrm{d}y, \\ bd_{\boldsymbol{k}}^{M} &= b_{\boldsymbol{k}}^1 + \frac{1}{\nu}\int \langle uv\rangle^M \phi_{\boldsymbol{k}}^{*1}\,\mathrm{d}y = b_{\boldsymbol{k}}^1 + d_{\boldsymbol{k}\boldsymbol{k}'}|a_{\boldsymbol{k}'}|^2; \end{aligned}$$

$bd_{\boldsymbol{k}}^{DNS}$ represents the exact extraction of energy from the mean shear in the DNS. This notation was chosen for consistency with that of the coefficients in the dynamical system. $bd_{\boldsymbol{k}}^{analytical}$ represents this extraction using (21) for the mean velocity profile and computing all quantities from the DNS $bd_{\boldsymbol{k}}^{M}$ is the restriction of $bd_{\boldsymbol{k}}^{analytical}$ to the truncation. It is the expression we use for the model. $b_{\boldsymbol{k}}^1$ and $d_{\boldsymbol{k}\boldsymbol{k}'}$ are computed from the empirical eigenfunctions, $|a_{\boldsymbol{k}}|^2$ is extracted from the DNS. All three terms are purely real since the first two components of streamwise-invariant eigenfunctions are real (Aubry (1987)).

We computed the time average of these three terms. We examined the feedback terms $fd_{\boldsymbol{k}} = bd_{\boldsymbol{k}} - b_{\boldsymbol{k}}^1$ and computed their standard deviation std$(fd_{\boldsymbol{k}})$. Results are summarized in table 2. The average energy extraction $\overline{bd_{\boldsymbol{k}}}$ seems not too badly estimated. The analytical expression slightly overestimates the mean extraction. Since stationarity was assumed when deriving the expression (see equation (7)), this means that the neglected temporal variations of the mean velocity profile $\partial U/\partial t$ are globally negative, or equivalently that its negative variations are stronger than its positive ones. This corresponds well to what is observed in the wall layer: strong ejections of low-momentum fluid versus gentle sweep-like motions. However, the time-averaged extraction of energy from the mean shear in the model tends to be underestimated. This is presumably because the first structure captures more than 100% of the Reynolds stress which makes a negative contribution to the energy extraction. Moin & Moser found that their first eigenfunction, which looks very much like ours,

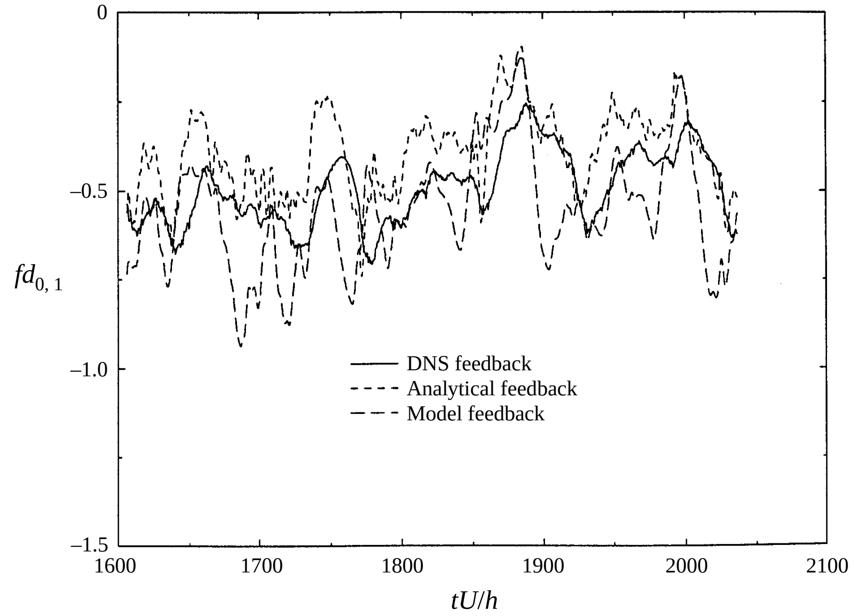

FIGURE 9. Mean velocity feedback for the POD mode $a_{0,1}$.

accounted for 120% of the total Reynolds stress (higher-order structures made negative contributions). This also explains why the amplitude of the feedback variations $\mathrm{std}(fd_k)$ is overestimated. Note that the amplitude of the analytical feedback variations matches the simulation well. As more modes are included in the truncation, the model will agree more closely with the DNS.

Next, we computed the correlation coefficients between the different feedbacks. We find for both modes

$$\begin{aligned} C(fd_k^{DNS}, fd_k^{M}) &\approx 0.45,\\ C(fd_k^{DNS}, fd_k^{analytical}) &\approx 0.70,\\ C(fd_k^{M}, fd_k^{analytical}) &\approx 0.70. \end{aligned}$$

We observe that there is a good correlation between the variations of the analytical and the modelled feedbacks. Although the analytical feedback gives a good representation of the mean flow behaviour, the modelled feedback seems to catch only some of it. Our model supposes that the effect of the large scales on the mean velocity profile is instantaneous, which is not very realistic. Figure 9 shows the time evolution of the three different feedback terms for the first mode (those for the second mode look very much the same). Clearly the modelled feedbacks are faster than the DNS. It takes some time for the mean velocity profile to be affected by the growth or collapse of the coherent structures. We recomputed the correlations, allowing for the DNS term to be positively delayed. We find for both modes

$$\begin{aligned} C_{max}(fd_k^{DNS}(t+\Delta), fd_k^{M}(t)) &\approx 0.71 \quad \text{for} \quad \Delta^+ = 110 \quad (\Delta U/h \approx 14),\\ C_{max}(fd_k^{DNS}(t+\Delta), fd_k^{analytical}(t)) &\approx 0.86 \quad \text{for} \quad \Delta^+ = 70 \quad (\Delta U/h \approx 8.5). \end{aligned}$$

The feedback will therefore be quite adequate if a response time is incorporated in the model for the mean velocity profile. Note that the delay is longer when only large scales are included since the final stage of a burst and the corresponding production of Reynolds stress will involve predominantly small scales (see also §6).

5.2. *The small-scale stress tensor*

In our model, we assume that the anisotropic part of the small-scale stress tensor is proportional to the strain rate of the large scales, i.e. that

$$\hat{\tau}_{ij>\boldsymbol{k}} = 2\nu_T \hat{s}_{ij<\boldsymbol{k}}, \tag{23}$$

where $\hat{\tau}_{ij>\boldsymbol{k}}$ is the Fourier transform of the unresolved small-scale tensor $\tau_{ij>}$ and $\hat{s}_{ij<\boldsymbol{k}}$ is the Fourier transform of the resolved strain rate tensor $s_{ij<}$ defined in §3.

The contribution of the small-scale stress tensor to the evolution equation of the POD modes is

$$S_{\boldsymbol{k}} = \int (\hat{\tau}_{ij,j})^{DNS}_{\underline{k}} \phi^{*i}_{\underline{k}} \, \mathrm{d}y \tag{24}$$

which is modelled by a term

$$-\alpha \nu_T b_{\boldsymbol{k}}^2 a_{\boldsymbol{k}}$$

in the low-dimensional system. In the model, α is held constant. In the DNS α should vary with time and also with the wavenumber $\boldsymbol{k}$. We first investigate the proportionality relationship. We compute the correlation coefficient between the modes $a_{0,k}$ and the small-scale stress tensor contribution $S_{\boldsymbol{k}}$. We find that this coefficient is about -0.7 for both modes. This supports remarkably well our crude eddy viscosity hypothesis. Once again, the agreement should be closer as the resolution increases.

Let us define $\alpha_{\boldsymbol{k}}$ such that

$$-\alpha_{\boldsymbol{k}} \nu_T b_{\boldsymbol{k}}^2 a_{\boldsymbol{k}} = S_{\boldsymbol{k}}. \tag{25}$$

We find

$$\|\alpha_{0,2} \nu_T b_{0,2}^2\| \approx 6 \|\alpha_{0,1} \nu_T b_{0,1}^2\|. \tag{26}$$

As expected, the dissipation to the small scales increases with the wavenumber. The values of $b_{\boldsymbol{k}}^2$, and in particular the ratio $b_{0,1}^2/b_{0,2}^2$ computed from the empirical eigenfunctions should be viewed with caution since they contain the second derivative of eigenfunctions and therefore cannot be computed very precisely. Let us determine a characteristic value $\alpha_{\boldsymbol{k}}^{char}$ for each mode. We use a least-squares fit and therefore define $\alpha_{\boldsymbol{k}}^{char}$ to be the value of $\alpha_{\boldsymbol{k}}$ for which the error between the DNS term and its representation in the model $e_{\boldsymbol{k}} = \|S_{\boldsymbol{k}} + \alpha_{\boldsymbol{k}} b_{\boldsymbol{k}}^2 \nu_T a_{\boldsymbol{k}}\|$ is minimum. This implies

$$\left. \frac{\partial e_{\boldsymbol{k}}}{\partial \alpha_{\boldsymbol{k}}} \right|_{\alpha_{\boldsymbol{k}}^{char}} = 0, \tag{27}$$

that is

$$\langle -b_{\boldsymbol{k}}^2 \nu_T a_{\boldsymbol{k}} | (S_{\boldsymbol{k}} - \alpha_{\boldsymbol{k}}^{char} b_{\boldsymbol{k}}^2 \nu_T a_{\boldsymbol{k}}) \rangle = 0. \tag{28}$$

Finally,

$$\alpha_{\boldsymbol{k}}^{char} b_{\boldsymbol{k}}^2 \nu_T = \frac{\displaystyle\int Re[S_{\boldsymbol{k}} a_{\boldsymbol{k}}^*] \, \mathrm{d}t}{\displaystyle\int a_{\boldsymbol{k}} a_{\boldsymbol{k}}^* \, \mathrm{d}t}. \tag{29}$$

Numerically,

$$\alpha_{\boldsymbol{k}}^{char} = \begin{pmatrix} 0.12 \\ 0.48 \end{pmatrix}.$$

To remove the dependence of the Heisenberg parameter on $\boldsymbol{k}$, we define by analogy with the theoretical estimates the parameter α_{both} satisfying

$$(2b_{0,1}^2 + b_{0,2}^2)\nu_T\alpha_{both} = 2\alpha_{0,1}\nu_T b_{0,1}^2 + \alpha_{0,2}\nu_T b_{0,2}^2; \tag{30}$$

α_{both} characterizes the variations of the theoretical modulus of the travelling wave due to changes in the Heisenberg parameter. The variations of α_{both} with time are shown in figure 10(*a*). The dominant characteristic of α_{both} is its strongly intermittent, spiky behaviour. Comparing figures 11(*a*) and 10(*a*), there is a clear correspondence between excursions of α_{both} and peaks in the wall shear history. The vertical lines correspond to local maxima, which we will relate to bursts and study in greater detail in §6. Figure 10(*b*) and figure 11(*b*) respectively show the variations of α_{both} and of the wall shear for the time sequence corresponding to the phase portrait of figure 8 in §4. The slowing down of the trajectory corresponds to an increase of $\|S_{\boldsymbol{k}}\|$ and a peak in the wall shear.

It then appears possible to link the change in dynamical behaviour of the POD modes with values of the energy transfer. When the Heisenberg parameter α is relatively low, the solution approaches a travelling wave, which corresponds physically to a pair of rolls slowly drifting in the spanwise direction. As α increases sharply, the drift of the rolls decreases and eventually becomes zero; in the bifurcation diagram, the travelling wave coalesces with a fixed point. This corresponds to a loss of energy for the zero streamwise modes reminiscent of the one observed in the even subspace of the ten-dimensional model at the initiation of a burst. We emphasize the fact that the bifurcation in the zero streamwise subspace does not exhibit *per se* the strong features associated with the bursting event in physical space. The 'spike' in the Heisenberg parameter constitutes a more tangible ingredient of bursting. We believe that the drift cancellation is only the signature of the excursion occurring transversally to the subspace spanned by our truncation. Note that for reasons discussed below in §5.3, the slowing down of the trajectory may not always coincide exactly with the peak in α.

Intermittency therefore appears in the model in a natural albeit indirect way, through the variations of a single free parameter α. This is equivalent to acknowledging implicitly the existence of higher modes. To be successful, a low-dimensional approach requires that a relatively low number of modes will introduce enough physics in the flow. Figure 12 shows the global energy transfer – the right-hand side of equation (30) proportional to α_{both} – including and excluding the first streamwise modes. Clearly a large part of the transfer goes directly to these modes, another manifestation of the cascade process. The mean and standard deviation of α_{both} are respectively decreased by 50% and 30% when these modes are omitted. There is then good reason to hope that a model including an extra few streamwise modes will capture intermittency. This will be the object of future study.

5.3. *Higher-order wall-normal eigenmodes*

We have seen in equation (12) that the modes $a_{\boldsymbol{k}}^n \in H(0,2,1)$ contribute to the linear and the quadratic terms. Our model does not account for these contributions. However, the cascade process being three-dimensional, energy transfers between low-order and high-order coherent structures are not likely to be negligible.

The full equations can be written as

$$\dot{a}_{\boldsymbol{k}} = \mathrm{RHS}_{\boldsymbol{k}}^{all} = L_{\boldsymbol{k}}^{all} + Q_{\boldsymbol{k}}^{all} + S_{\boldsymbol{k}}, \tag{31}$$

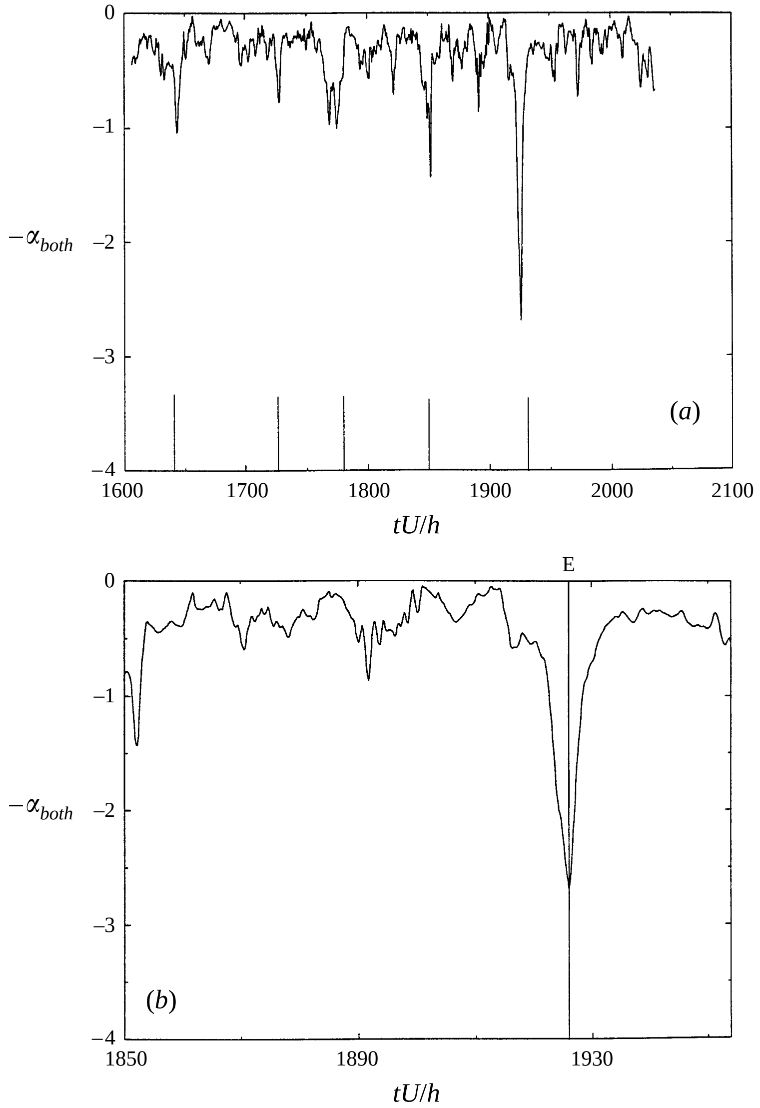

FIGURE 10. (*a*) Global Heisenberg parameter. (*b*) Heisenberg parameter for each mode – a blow up.

where

$$S_k = \int \hat{\tau}_{ij,j}\phi_k^{*i}\,\mathrm{d}y, \quad L_k^{all} = -\int \mathrm{d}U/\mathrm{d}y\, v\phi_k^{*1}\,\mathrm{d}y, \quad Q_k^{all} = -\int (u^i_{k'}u^j_{k-k'})_{,j}\phi_k^{*i}\,\mathrm{d}y$$

and all other terms are neglected.

We then derive our model from the truncated equations

$$\dot{a}_k = \mathrm{RHS}_k^1 = L_k^1 + Q_k^1 + S_k, \tag{32}$$

where

$$L_k^1 = -a_k \int \mathrm{d}U/\mathrm{d}y\, \phi_k^2 \phi_k^{*1}\,\mathrm{d}y, \quad Q_k^1 = -a_{k'}a_{k-k'} \int (\phi^i_{k'}\phi^j_{k-k'})_{,j}\phi_k^{*i}\,\mathrm{d}y.$$

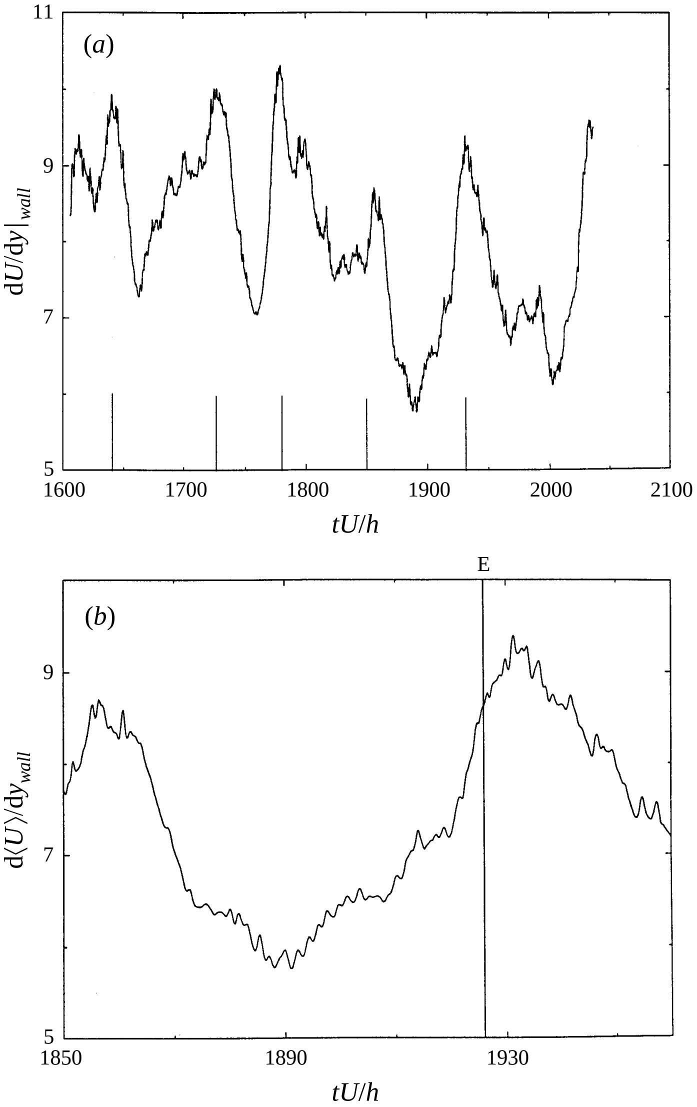

FIGURE 11. (*a*) Wall shear history. (*b*) Wall shear history – a blow up.

We finally obtain the model equations

$$\dot{a}_k = \mathrm{RHS}_k^M = L_k^M + Q_k^M + S_k^M, \tag{33}$$

where

$$L_k^M = (b_k^1 + d_{kk'}|a_{k'}|^2)a_k, \quad Q_k^M = c_{k'k-k'}a_{k'}a_{k-k'}, \quad S_k^M = -\alpha_k^M \nu_T b_k^2 a_k,$$

where α_k^M is constant in time.

We want to compare all three formulations (31), (32) and (33). We first observe that we have already compared the modelled and the truncated equations, since $Q_k^M = Q_k^1$ and comparison of expressions for L_k and S_k has been carried out in the two preceding subsections.

To compare the full and the truncated equations, we compute intensities and correlation coefficients between corresponding terms in each formulation. Results

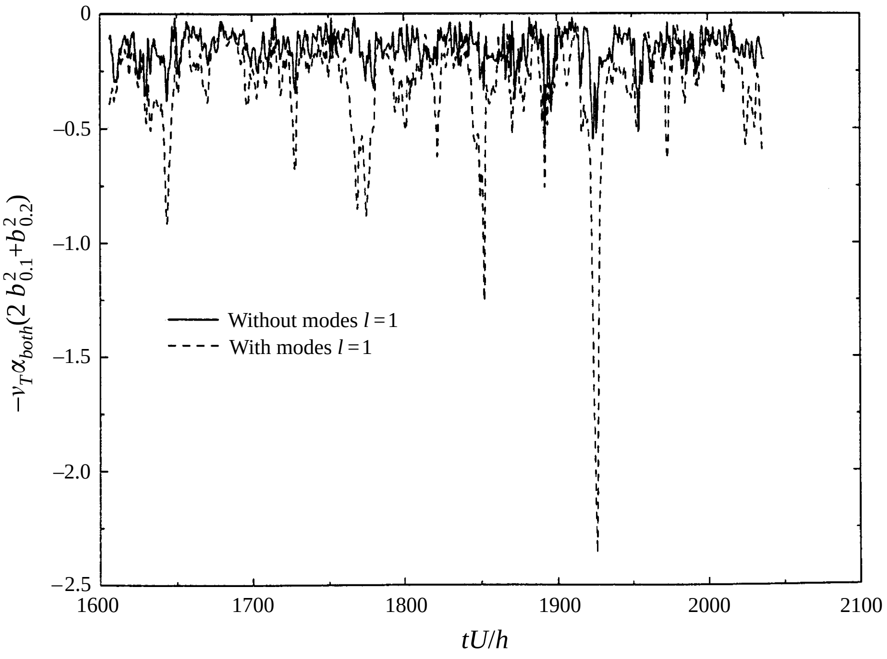

FIGURE 12. Contribution of the first streamwise modes to energy transfer.

$\Vert L_k^{all}\Vert = (0.11, 0.15)^T$	$\Vert L_k^1\Vert = (0.15, 0.08)^T$	$C(L_k^{all}, L_k^1) = (0.92, -0.30)^T$
$\Vert Q_k^{all}\Vert = (0.02, 0.55)^T$	$\Vert Q_k^1\Vert = (0.04, 0.34)^T$	$C(Q_k^{all}, Q_k^1) = (-0.33, 0.93)^T$
$\Vert \mathrm{RHS}_k^{all}\Vert = (0.11, 0.36)^T$	$\Vert \mathrm{RHS}_k^1\Vert = (0.09, 0.32)^T$	$C(\mathrm{RHS}_k^{all}, \mathrm{RHS}_k^1) = (0.74, 0.80)^T$

TABLE 3. Characteristic intensities.

are given in table 3. The dominant terms in both formulations are source terms ($\Vert S_k\Vert = (0.03,\ 0.17)^T$). In a cascade-like fashion, the dominant term in the equation for the first mode $a_{0,1}$ is the linear term $L_{0,1}$ which represents the extraction of energy from the mean shear. In the equation for the second mode $a_{0,2}$, the dominant term is the quadratic term $Q_{0,2}$ which represents a gain of energy from the first mode (conversely the quadratic term $Q_{0,1}$ represents a loss of energy to the second mode). These dominant terms are relatively little affected by the inclusion or exclusion of higher wall-normal eigenmodes in their formulation. Overall the full equations are relatively close to their truncated counterparts.

To compare the full equations to the model, we determine by least-squares fit the values of the model coefficients which would best approximate the full terms. The interaction with the mean shear is computed globally in the DNS, so that only the sum of the linear and the cubic terms in the model is accessible. We choose to determine the linear term ${b_k^1}^{all}$ by looking for a linear approximation to $L_k^{all} - f d_k^M a_k = L_k^{all} - d_{kk'}|a_{k'}|^2 a_k$. We then compare the values for the linear and the quadratic terms to those originally computed from the empirical eigenfunctions. Our findings are summarized in table 4. The agreement between the different coefficients is relatively good. The effect of the higher eigenmodes is to reinforce the lowest-order first and second POD modes through respectively linear and quadratic interactions.

$b_k^{1\ all} = (0.76, 0.65)^T$	$b_k^{1\ M} = (0.62, 0.65)^T$
$(c_{-1,2}, c_{1,1})^{all} = (0.01, -0.32)^T$	$(c_{-1,2}, c_{1,1})^{M} = (0.04, -0.20)^T$

TABLE 4. Projected coefficients.

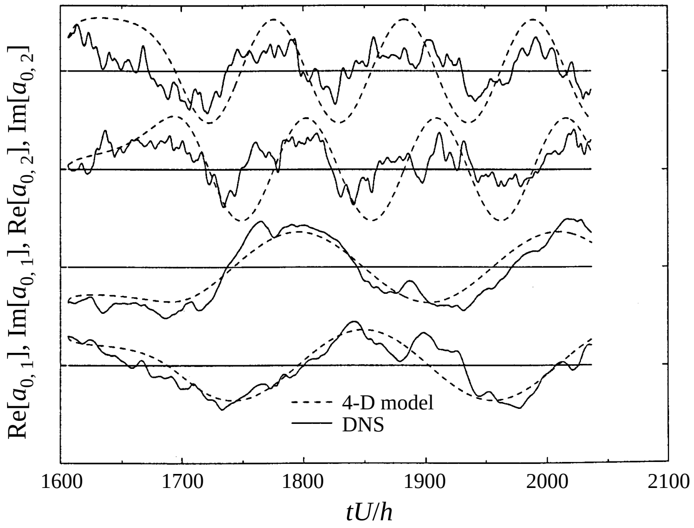

FIGURE 13. Comparison of DNS and model time histories.

6. Direct comparison of the low-dimensional system and the DNS

6.1. *Long-term behaviour*

We address the following question: how accurately can our model predict the large-scale behaviour of the POD modes? The form of the model, and in particular the values of the coefficients computed in §4 from the empirical eigenfunctions, have now been validated through examination of the modelling assumptions. It only remains to determine an appropriate value for the Heisenberg parameter α. We adjust this parameter slightly, using for each mode a value within a few percent of the value α_k^{char} determined from the DNS in §5.2. We find that the corresponding system lies in a region close to the bifurcation point, so that small changes in α will substantiallly alter the characteristics of the solution. This supports Lumley & Podvin's (1996) argument that variations in α should create a strong feedback in order to maintain the boundary layer in its equilibrium state. The fluctuations of the period of the travelling wave correspond to variations in α of less than 1%, which is superior to the degree of accuracy with which we can expect to obtain the coefficients of the equations.

We integrate the low-dimensional model from an arbitrary value of the POD modes in the DNS. Figure 13 presents a comparison of the result of the integration and the true time histories of the POD modes. There is relatively good agreement between the large-scale behaviour of the actual POD modes and its prediction by our basic model.

We now return to the question of intermittency. So far, changes in dynamical behaviour for the POD modes were associated with temporal variations in the parameter α which characterizes the transfer to the small scales. Studying the modelling assumptions shows that this is only a crude picture. The discrepancy between our assumptions and the DNS introduces other substantial variations in the model. For our model to be relevant, the variation in α should be representative of the total variation in the low-dimensional equations. As a first estimation, we express these variations as the difference between the intensity of the full DNS term and that of its modelled approximation obtained by least-squares fit. The variation in α will then be represented by

$$|S_{\boldsymbol{k}}|^2 - |\alpha_{\boldsymbol{k}}^{char} b_{\boldsymbol{k}}^2 \nu_T a_{\boldsymbol{k}}|^2,$$

where $||$ denotes the complex modulus. We use a crude linear approximation for the total right-hand side $\mathrm{RHS}_{\boldsymbol{k}}^{all}$, so that the total variation can be written as

$$|\mathrm{RHS}_{\boldsymbol{k}}^{all}|^2 - |T_{\boldsymbol{k}}^{char} a_{\boldsymbol{k}}|^2,$$

where $T_{\boldsymbol{k}}^{char}$ is the constant which minimizes $\|\mathrm{RHS}_{\boldsymbol{k}}^{all} - T_{\boldsymbol{k}} a_{\boldsymbol{k}}\|^2$. Note that this approximation would be exact if the DNS solution were a pure travelling wave. The different variations for each mode are shown in figures 14(*a*) and 14(*b*). Given the relatively small magnitude of the variations of α, it is clear that dynamical changes will not be solely determined by nor coincide exactly with excursions in the Heisenberg parameter. However, there is a sufficient amount of correlation – the correlation coefficients between the two curves for mode $(0,1)$ and $(0,2)$ are respectively 0.7 and 0.4 – to support at least partially an α-based approach.

6.2. *Intermittency*

To further strengthen the relationship between our model and intermittency in the MFU, we monitored time histories of standard bursting indicators for the flow along with relevant low-dimensional parameters. Special events were identified. We examined many of them and feel reasonably confident in the typical character of the observations reported below.

The bursting process usually described in experiments using fixed probes – Eulerian description – involves an isolated region of fluid which suddenly leaves a relatively quiescent state to experience a violent, disorganized ('chaotic') motion. More recent investigations Hunt (1988) made in a Lagrangian frame suggest that rather the structures diffuse slowly into incoherent motions. It has even been advanced that what was previously viewed as a burst corresponds in fact to the mere passage of a structure by the probe. Since our interest lies in the dynamical changes associated with the generation of turbulence, our viewpoint here is slightly different. It is based on the general idea that the flow does go through different states of excitation, the succession of which constitutes the bursting process.

In the conventional Eulerian description, standard characteristics of turbulence such as turbulence production are much more intense during bursts than on average. Jimenez & Moin showed that in that respect, there was always some point bursting at any time in the box. However they also observed variations of substantial magnitude in the overall bursting activity of the box. Monitoring globally defined quantities which on a local scale are usually associated with the bursting process – such as the spatially averaged wall shear or the maximum vorticity production over the box – they identified a regeneration cycle common to all these quantities. Each quantity reached its maximum over a period of time short relative to the length of the cycle.

Figure 15 shows the total production of turbulence $P = -\int_{y=0}^{y=40+} \mathrm{d}U/\mathrm{d}y \langle uv \rangle \,\mathrm{d}y$, while figure 11(*a*) shows the corresponding drag history at the wall. Figure 16 shows

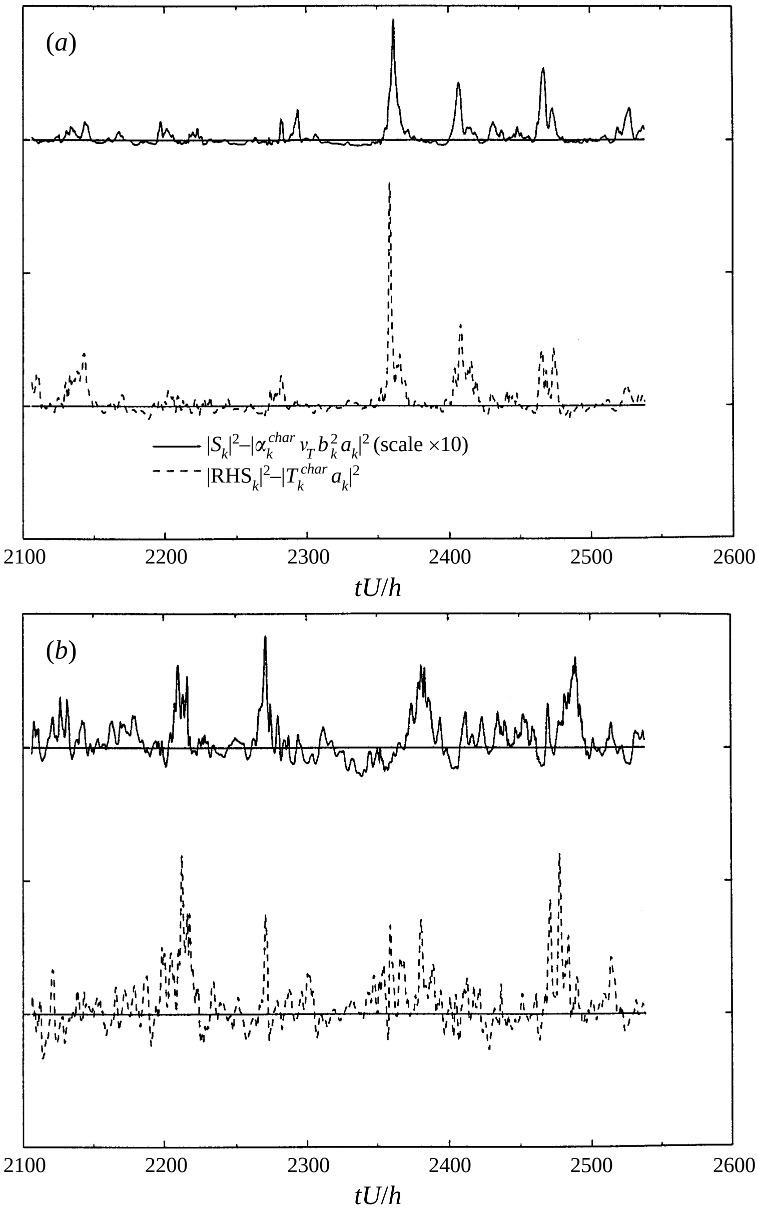

FIGURE 14. Comparison of variations in α and total variations: (*a*) first mode $a_{0,1}$, (*b*) second mode $a_{0,2}$.

the amplitude of the dominant POD mode $|a_{0,1}|^2$, while figure 10(*a*) shows the time evolution of the parameter α_{both}. Additionally, we monitored the amplitude of the first streamwise modes $\sum_{|k|\leqslant 2}|a_{1,k}|^2$ towards which the streamwise rolls transfer a major part of their energy.

The production and the drag history are extremely well correlated with a delay of about 50 wall units for the drag history. The amplitude of $|a_{0,1}|^2$ is also well correlated with those curves, allowing for a longer delay of 120 units. All this is consistent with the following picture: the primary effect of the streamwise rolls is

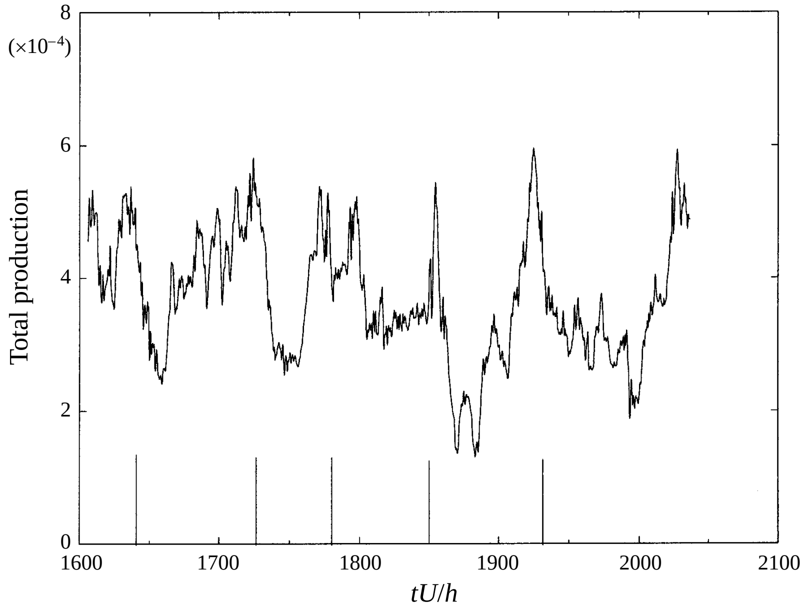

FIGURE 15. Production of turbulence integrated over the wall layer $-\int \mathrm{d}U/\mathrm{d}y\langle uv\rangle$.

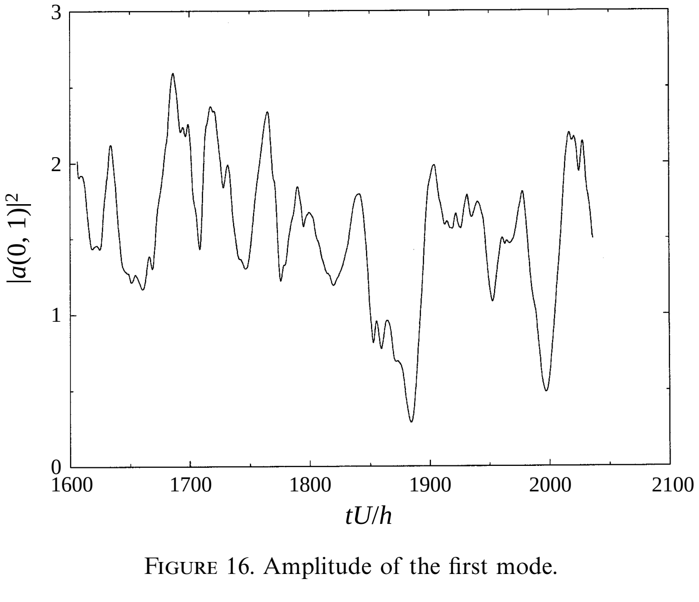

FIGURE 16. Amplitude of the first mode.

to lift low-momentum fluid into the core of the flow, during which time the drag at the wall is low. Then some instability mechanism – possibly secondary instability (see Robinson 1991) – gives rise to high-wavenumber turbulence and subsequent production of turbulence. Since turbulence is fully developed, the vertical extent of fluid motion in the boundary layer corresponds to the channel half-height h. Then high-speed momentum is swept down towards the wall in a time about h/u_*, where h is the channel half-height and the friction velocity u_* characterizes the normal turbulent fluctuations. Since the half-channel is about 180 wall units, this will mean a delay of roughly 90 units, which agrees with our observations. Note that this scaling corresponds to a mixture of outer and inner units as proposed in Aubry *et al.* (1988).

The dependence relationships which exist between the various 'burst indicators' determine a definite pattern for their activation. We focus on three representative events. The monitored quantities reported in figure 17(*a–c*) are the normalized variations of the amplitude of the dominant POD mode $a_{0,1}$, the amplitude of the first streamwise POD modes, the Heisenberg parameter α_{both}, the production of turbulence in the wall layer and the wall shear history. These quantities reach their maximum in the order just mentioned. Note how the peaks in the production are closely related to the increase in amplitude of the first streamwise modes and the Heisenberg parameter. It seems that the streamwise rolls are the fundamental structures in the bursting process, in that their intensity predetermines the violence of the burst. Destabilization occurs with the growth of modes breaking the streamwise invariance. As energy is being transferred to higher modes, small-scale motion is generated, which results in intensive production of turbulence. The event ends when the wall shear reaches its peak, thereby signalling the completion of the sweep.

It is generally understood that the bursting process is primarily related to a spanwise inflectional profile of the streamwise velocity. This was notably observed in the experiments of Swearingen & Blackwelder (1987). More recently, Waleffe and co-workers have produced a nonlinear model (Waleffe 1995; Hamilton *et al.* 1995) in which instability is due to streamwise streaks, generated by streamwise vortices. In their new book, Holmes *et al.* (1996) show how this mechanism – in particular the regeneration of streamwise vortices – is fully consistent with the low-dimensional paradigm. Although the role they play in the bursting process is still unclear, inflection points are also observed in the normal direction. Corino & Brodkey (1969), Blackwelder & Kaplan (1976) and Kline *et al.* (1967) report the appearance of these inflectional profiles as an exclusive characteristic of bursting times. We monitored horizontally averaged velocity profiles and found evidence of inflectional regions during excitation periods of the regeneration cycle. Profiles corresponding to our three events are shown in figure 18(*a–c*).

The intermittency cycle of the MFU does seem to correspond to that captured by our low-dimensional model. Its features are very similar to that of the bursting process described in experiments. The only major discrepancy is the anomalously long time scale. It is likely that this is an artefact of the computation. Because of the box dimensions, we are always observing the regeneration of the same structure. Long bursting periods were also found to characterize the ten-dimensional model which represented a box of similar size. In the latter case, we found that a simple convection model restored the correct magnitude of the bursting frequency observed in experiments (Podvin *et al.* 1997).

7. Low-dimensional models and information recovery

7.1. *The context*

Implementation of feedback control strategies requires some knowledge of the time evolution of the flow. For instance, if the control is based on our low-dimensional approach, it will need to know the values of the dominant POD modes. The desired information may not be three-dimensional, but it will typically involve the interior of the flow, particularly the region where most of the turbulence is generated. For instance, Choi, Moin & Kim (1994) used a sucking/blowing control based on the value of the

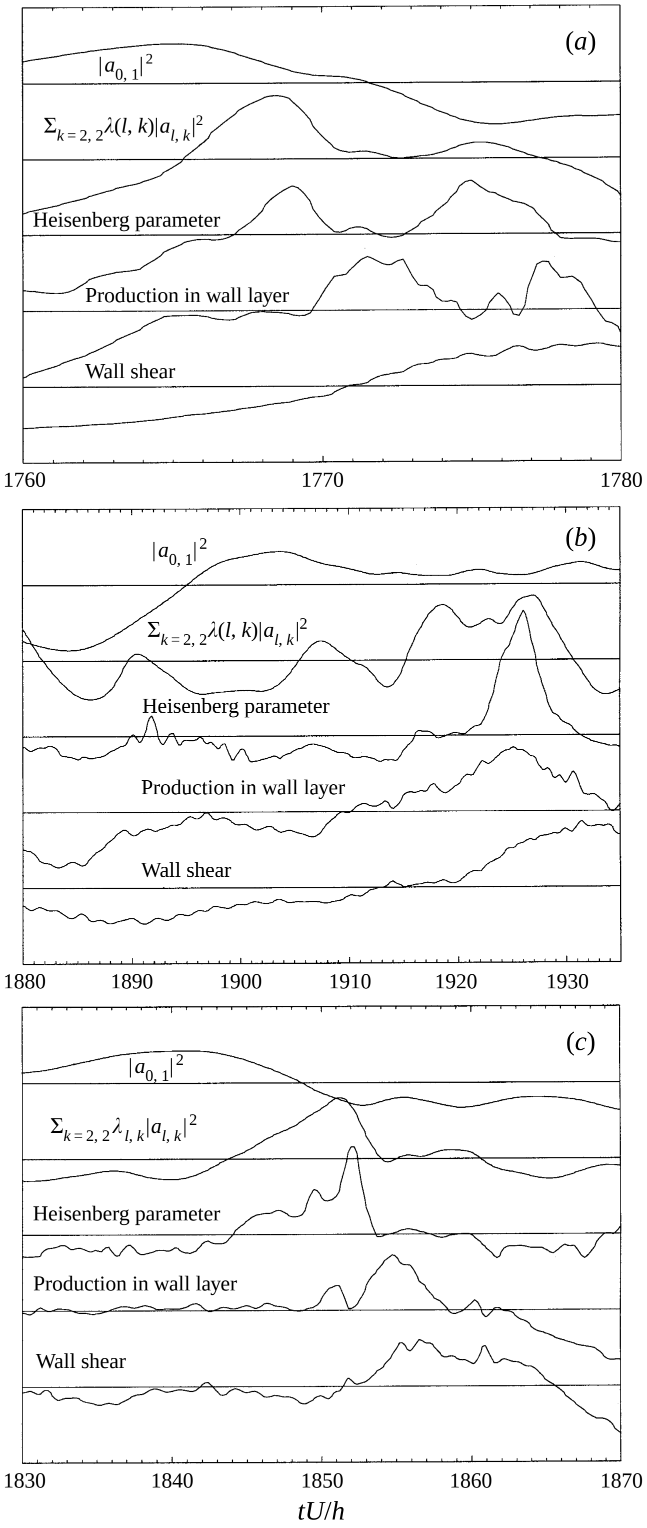

FIGURE 17. (*a*) Event 1, (*b*) Event 2, (*c*) Event 3.

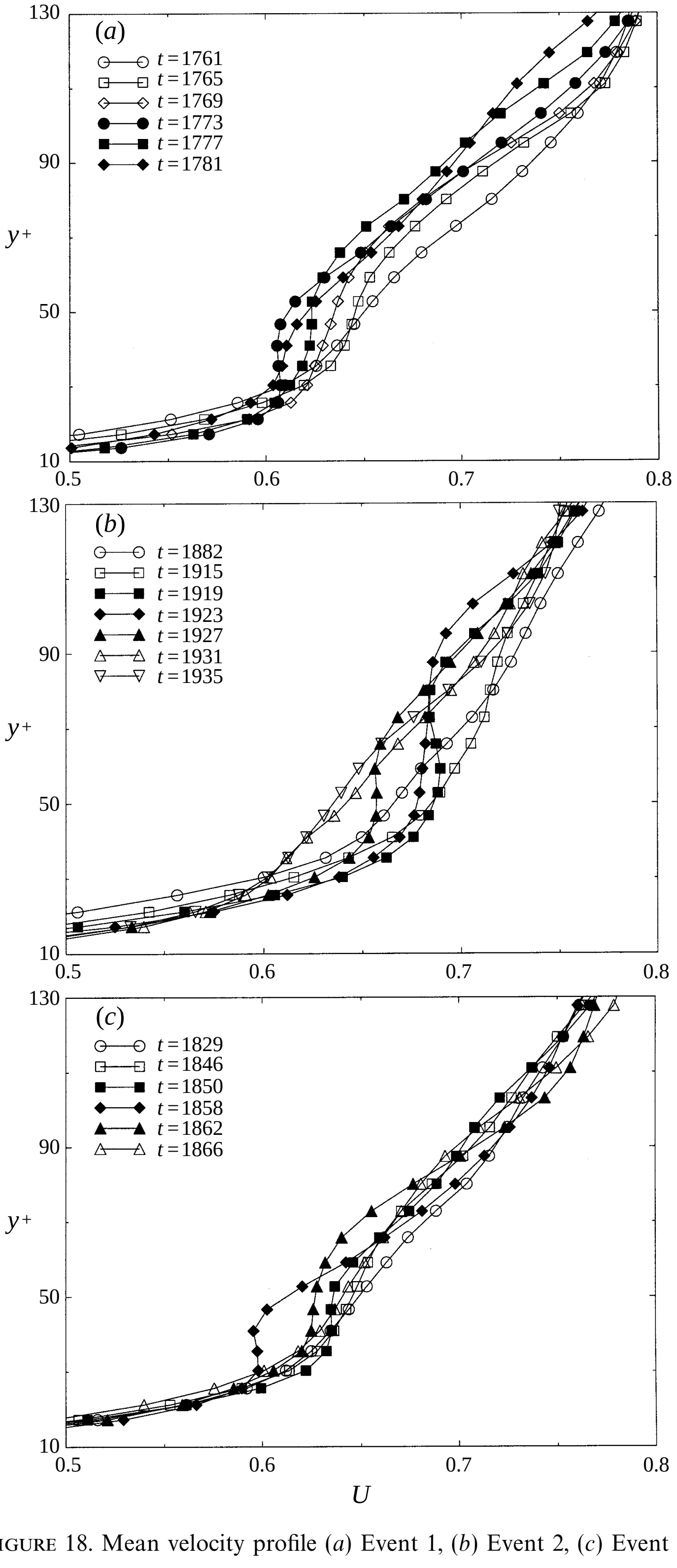

FIGURE 18. Mean velocity profile (*a*) Event 1, (*b*) Event 2, (*c*) Event 3.

cross-stream components of the velocity fields at some height – about 20 wall units – in the wall layer. This information can easily be obtained in a numerical simulation or with more difficulty from an experiment, but remains generally inaccessible in real life. Under realistic conditions, say an airplane wing, measurements will typically be made along an array of sensors located on the flow boundary. Partial information can dramatically affect the control performance. Choi *et al.* found that the 20% drag reduction obtained with full flow information dropped to 6% when using only wall information.

In addition, physical constraints impose a lower bound on the size of the sensors and therefore the spacing of the grid. These restrictions have been partially lifted due to the emergence in recent years of micromachinery and the fast development of micro-electro-mechanical systems (MEMS). See Gad-el-Hak (1994) for a review of these. A typical size for MEMS sensors is 30 μm, which allows a sensor spacing of about 100 μm. However, this is still a substantial scale at the high Reynolds numbers considered – typically 10^7 and a few 10^6 respectively for the aircraft and naval industry. A sensor spacing of 100 μm will represent a few tens of wall units in this range of Reynolds numbers. In contrast, the bursting process has been observed to involve typical spanwise scales of 20 wall units Corino & Brodkey (1969). Under these conditions, aliasing is not negligible. If δ is the grid spacing for the sensors, only wavenumbers smaller than a cut-off wavenumber $k_c = 1/2\delta$ will be recovered. Higher wavenumbers will be aliased to a smaller wavenumber such that the difference between the two wavenumbers is a multiple of twice the value of the cut-off wavenumber (Nyquist theorem).

The situation we have just described defines a general filtering problem: given a set of measurements at successive times up to time T, $\{Y_t\}_{0\leqslant t\leqslant T}$, estimate some related quantity at this time T, a_T. We now examine how classical solutions to this problem can be adapted to our particular case.

7.2. *The estimation problem*

Our goal is to recover the value of the POD modes of our two-mode model from measurements of the wall shear along a grid of realistic, i.e. relatively large, dimensions. The wavelengths of our two modes are respectively 185 and 92.5 wall units (+). Although we are not at this point directly interested in streamwise information, we found elsewhere that aliasing in the streamwise direction could significantly hamper the recovery of the streamwise-invariant modes and required using a two-dimensional array. The grid dimensions are 50 and 25 wall units in respectively the streamwise and spanwise directions. This represents a feasible set-up. Sensors located on that grid at the wall measure the instantaneous streamwise and spanwise components of the shear $\mathrm{d}u^{i=1,3}/\mathrm{d}y|_{wall}$. Using the POD decomposition for the wall shear, we have

$$\mathrm{d}\hat{u}_{\boldsymbol{k}}^{i=1,3}/\mathrm{d}y = \sum_{n=1}^{\infty}\sum_{q\in\mathscr{Z}} a_{\boldsymbol{k}+2q\boldsymbol{k}_c}\mathrm{d}\phi_{\boldsymbol{k}+2q\boldsymbol{k}_c}^{i=1,3}/\mathrm{d}y, \tag{34}$$

where $\mathrm{d}\hat{u}_{\boldsymbol{k}}/\mathrm{d}y$ represents the discrete Fourier transform for wavenumbers smaller than the cut-off wavenumber, i.e. $k^i \leqslant k_c^i$. The system can be rewritten as

$$\left.\begin{aligned}
\mathrm{d}\hat{u}_{0,1}^{1}/\mathrm{d}y|_{wall} &= a_{0,1}\mathrm{d}\phi_{0,1}^{1}/\mathrm{d}y|_{wall} + \eta_1^1,\\
\mathrm{d}\hat{u}_{0,1}^{3}/\mathrm{d}y|_{wall} &= a_{0,1}\mathrm{d}\phi_{0,1}^{3}/\mathrm{d}y|_{wall} + \eta_1^3,\\
\mathrm{d}\hat{u}_{0,2}^{1}/\mathrm{d}y|_{wall} &= a_{0,2}\mathrm{d}\phi_{0,1}^{1}/\mathrm{d}y|_{wall} + \eta_2^1,\\
\mathrm{d}\hat{u}_{0,2}^{3}/\mathrm{d}y|_{wall} &= a_{0,2}\mathrm{d}\phi_{0,2}^{3}/\mathrm{d}y|_{wall} + \eta_2^3,
\end{aligned}\right\} \tag{35}$$

where $\eta_k^{i=1,3}$ represents the perturbation due to the higher modes.

We now define the solution $a_{0,k}^{measured}$ directly extracted from the instantaneous measurements. We reduce the system (35) by taking for each mode a weighted average of the streamwise and the spanwise equations. We then solve for a, neglecting higher-order terms. We have

$$a_{0,k}^{measured} = \left(\beta \frac{\mathrm{d}\hat{u}_{0,k}^{1}/\mathrm{d}y}{\mathrm{d}\phi_{0,k}^{1}/\mathrm{d}y} + (1-\beta) \frac{\mathrm{d}\hat{u}_{0,k}^{3}/\mathrm{d}y}{\mathrm{d}\phi_{0,k}^{3}/\mathrm{d}y} \right) \Bigg|_{wall} . \tag{36}$$

We found that shifting the weight β towards the spanwise component improved our direct estimation.

In this particular situation, additional information is provided by the low-dimensional evolution equations. In the case where both measurements and evolution equations are linear and the disturbances are pure white noise, a recursive algorithm to solve this problem has been derived by Kalman (1960). The key idea of the Kalman filter is to provide estimates for the unknowns by combining dynamical information with instantaneous measurements. The estimates are advanced in time using modified evolution equations which are adjusted using feedback from the measurements.

Following Kalman's idea, we developed the following filtering procedure. At each time step, we determined the first mode directly from the measurements $a_{0,1}^{measured}$ and low-pass filtered the result. We used a crude moving average based on previous and current measurements. The length of the window was about 40 wall time units. Since the streamwise length of the box is about 400 wall units and the average convection velocity in the wall layer is roughly $10u_*$, the averaging time represents the time it will take a particle of fluid in the wall layer to go through the box. In the minimal flow unit, the same streak is constantly re-entering the box. In real flows, since the typical length of a streak is between 400 and 1000 wall units Kim *et al.* (1971), this corresponds to averaging over at most individual streaks.

To recover the second mode, we assumed that the four-dimensional system adapts itself sufficiently fast to changes in the evolution equations to remain close to its equilibrium. We therefore assumed a local travelling wave structure for the solution of the system. The two modes were supposed to be phase-locked with the observed phase difference of π. The amplitudes of the modes were assumed to be correlated. Additionally, we used time-averaged statistics to determine the mean ratio of the amplitudes. The second mode was then reconstituted from the filtered estimation of the first mode, following

$$a_{0,2}^{estimated} = \overline{\frac{|a_{0,2}|}{|a_{0,1)}|}} |a_{0,1}^{estimated}| \mathrm{e}^{\mathrm{i}\pi} \mathrm{e}^{2\mathrm{i}\mathrm{Arg}[a_{0,1}^{estimated}]} . \tag{37}$$

Results for the two modes (four components in real space) are shown in figures 19(*a*–*d*). The true state represents the POD mode computed in the DNS. The measured state has already been defined. The estimated state is the result of our estimation procedure. The improvement for both modes is considerable. In particular, aliasing affects the second mode so strongly that standard filtering techniques will not be effective. Note that since the first mode is directly determined from the measurements, only very general assumptions on the form of the solution are required. The success of this very simple approach under conditions as realistic as those of this basic flow illustrates clearly the versatility of low-dimensional models.

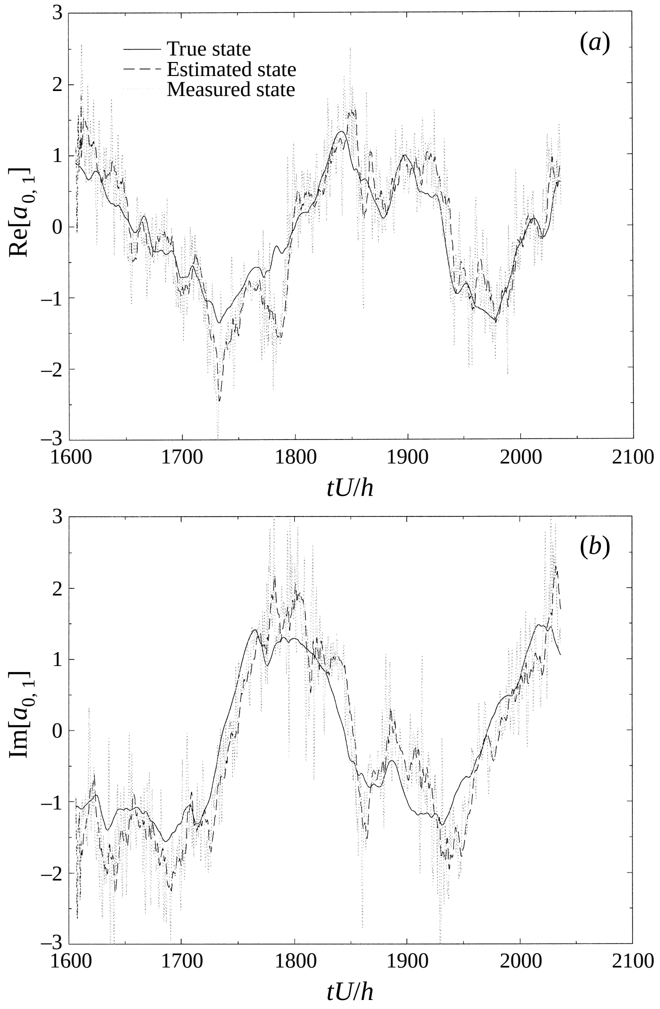

FIGURE 19 (a, b). For caption see facing page.

8. Conclusion

This work represents the first quantitative estimation of POD low-dimensional models for the wall layer. It was performed in the context of the MFU which represents the domain spanned by the two-mode model already studied in Armbruster *et al.* (1988) and Stone (1989). POD time histories from the model were compared to those extracted from the flow. Modelling assumptions were checked against the numerical simulation. The agreement is generally good, and is expected to improve with larger truncations. Two aspects of the comparison are worth emphasizing. Firstly, the model successfully predicts the long-term behaviour of the modes. Secondly, a close correspondence exists between the regeneration cycle of the MFU and intermittency in the low-dimensional model.

A relevant question is how this study can be related to full-scale turbulence. We have carried out our comparison in an artificial frame, which corresponds to the mathematical domain of our low-dimensional model, but differs from a full flow sim-

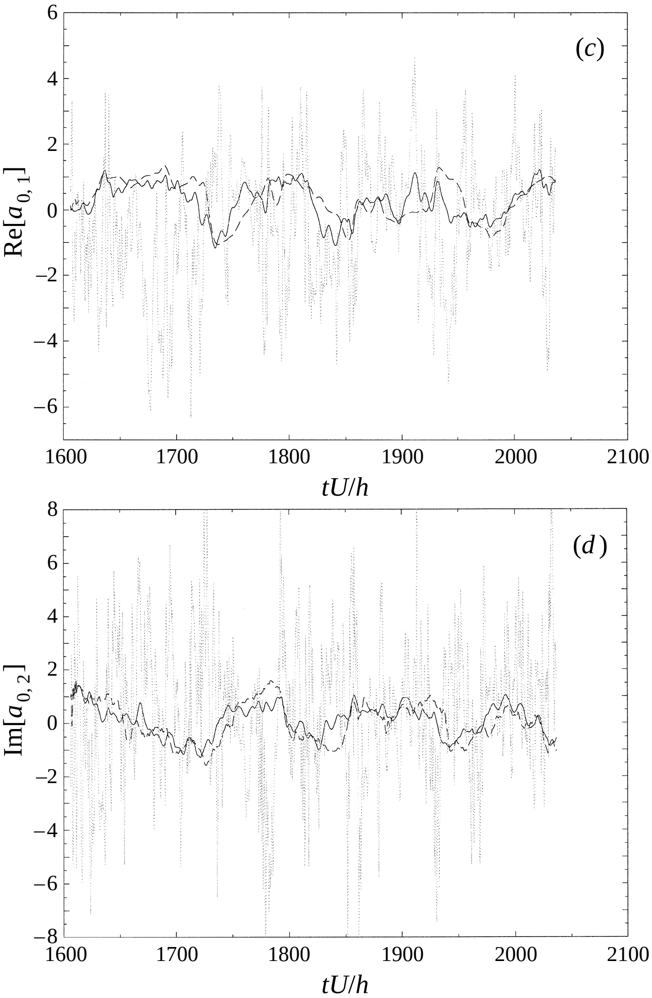

FIGURE 19. Estimation of (*a*) $\mathrm{Re}[a_{0,1}]$, (*b*) $\mathrm{Im}[a_{0,1}]$, (*c*) $Re[a_{0,2}]$, (*d*) $\mathrm{Im}[a_{0,2}]$ grid spacing $(\delta_1, \delta_3) = (50+, 25+)$.

ulation. The four-dimensional model reproduces the travelling wave observed in the MFU, yet travelling waves are not likely to be a persistent feature of a real turbulent flow. The intermittency described here presents features quite similar to the bursting phenomenon observed in a full DNS. Low-momentum fluid is ejected from the wall region, associated after a slight lag with production of high-wavenumber turbulence, and still later with the increase of wall stress. However, the intermittency mechanism exhibited by the four-dimensional model is of an implicit character. It corresponds to the temporal variations of the Heisenberg parameter which characterizes the energy transfer to the unresolved scales. In contrast, intermittency appears explicitly in the ten-dimensional model of Aubry *et al.* (1988). We believe that adding streamwise modes to the basic two-mode model will provide an explicit source of destabilization. The four-dimensional model by itself is unable to reproduce the kind of burst that the ten-dimensional model is capable of, for a constant value of α. The conclusion is then that the MFU is constrained by its small domain to produce a more limited behaviour than the full DNS, just as the four-dimensional model produces behaviour less rich than the ten-dimensional model, constrained by its lower dimension, but that ghosts of the full behaviour can be found in both the MFU and the four-dimensional model.

Supported in part by Contract No. F49620-92-J-0287 jointly funded by the US Air Force Office of Scientific Research (Control and Aerospace Programs), and the US Office of Naval Research, in part by Grant No. F49620-92-J-0038, funded by the US Air Force Office of Scientific Research (Aerospace Program), and in part by the Physical Oceanography Programs of the US National Science Foundation (Contract No. OCE-901 7882) and the US Office of Naval Research. (Grant No. N00014-92-J-1547).

REFERENCES

Armbruster, D., Guckenheimer, J. & Holmes, P. 1988 Heteroclinic cycles and modulated travelling waves in systems with o(2) symmetry. *Physica* D **29**, 257–282.

Aubry, N. 1987 A dynamical system/coherent structure approach to the fully developed turbulent wall layer. PhD thesis, Cornell University.

Aubry, N., Holmes, P., Lumley, J. L. & Stone, E. 1988 The dynamics of coherent structures in the wall region of the wall boundary layer. *J. Fluid Mech.* **192**, 115–173.

Bakewell, H. P. & Lumley, J. L. 1967 Viscous sublayer and adjacent wall region in turbulent pipe flow. *Phys. Fluids* **10**, 1880–1889.

Berkooz, G. 1991 Turbulence, coherent structures, and low dimensional models. PhD thesis, Cornell University.

Berkooz, G., Holmes, P. & Lumley, J. L. 1993*a* On the relation between low-dimensional models and the dynamics of coherent structures in the turbulent wall layer. *Theor. Comput. Fluid Dyn.* **4**, 265–269.

Berkooz, G., Holmes, P. & Lumley, J. L. 1993*b* The proper orthogonal decomposition in the analysis of turbulent flows. *Ann. Rev. Fluid Mech.* **25**, 539–575.

Blackwelder, R. F. & Kaplan R. E. 1976 On the wall structure of the turbulent boundary layer. *J. Fluid Mech.* **76**, 89–112.

Carlson, H. A. 1995 A dynamical system/coherent structure approach to the fully developed turbulent wall layer. PhD thesis, Cornell University.

Carlson, H. A. & Lumley J. L. 1996 Active control in the turbulent boundary layer of a minimal flow unit. *J. Fluid Mech.* **329**, 341–371.

Choi, H., Moin, P. & Kim, J. 1994 Active turbulence control for drag reduction in wall-bounded flows. *J. Fluid Mech.* **262**, 75–110.

Coller, B. D., Holmes, P. & Lumley, J. L. 1994 Control of bursting in turbulent boundary layers models. *Appl. Mech. Rev.* **47**, S139–S143.

Corino, E. R. & Brodkey, R. S. 1969 A visual investigation of the wall region in turbulent flow. *J. Fluid Mech.* **37**, 1–30.

Gad el Hak, M. 1994 Interactive control of turbulent boundary layers: A futuristic overview. *AIAA J.* **32**, 1753–1765.

Hamilton, J. M., Kim, J. & Waleffe, F. 1995 Regeneration mechanisms of near-wall turbulence structures. *J. Fluid Mech.* **287**, 317–348.

Herzog, S. 1986 The large scale structure in the near-wall region of turbulent pipe flow. PhD thesis, Cornell University.

Hinze, J. O. 1976 *Turbulence*. McGraw-Hill.

Holmes, P., Lumley, J. L. & Berkooz, G. 1996 *Turbulence, Coherent Structures, Dynamical Systems and Symmetry*. Cambridge University Press.

Hunt, J. C. R. 1988 Studying turbulence using direct numerical simulation: 1987 CTR NASA AMES/Stanford Summer Programme. *J. Fluid Mech.* **190**, 375–392.

Jimenez, J. & Moin, P. 1991 The minimal flow unit in near-wall turbulence. *J. Fluid Mech.* **225**, 213–240.

KALMAN, R. E. 1960 A new approach to linear filtering and prediction problems. *J. Basic Engng* **4**, 35–45.

KIM, H. T., KLINE, S. J. & REYNOLDS, W. C. 1971 The production of turbulence near a smooth wall in a turbulent boundary layer. *J. Fluid Mech.* **50**, 133–160.

KLINE, S. J., REYNOLDS, W. C., SCHRAUB, F. A. & RUNSTADLER, P. W. 1967 The structure of turbulent boundary layers. *J. Fluid Mech.* **30**, 741–773.

LUMLEY, J. L. 1967 The structure of inhomogeneous turbulent flows. In *Atmospheric Turbulence and Radio Wave Propagation* (ed. A. M. Yaglom & V. I. Tatarski), pp. 221–227. Nauka, Moscow.

LUMLEY, J. L. & PODVIN, B. 1996 Dynamical systems theory and extra rates of strain in turbulent flows. *J. Exp. Thermal Fluid Sci.* **267**, 1–10.

MOIN, P. & MOSER, R. 1989 Characteristic-eddy decomposition of turbulence in a channel. *J. Fluid Mech.* **200**, 471–509.

PODVIN, B., GIBSON, J., BERKOOZ, G. & LUMLEY, J. L. 1997 Lagrangian and eulerian view of the bursting period. *Phys. Fluids* **9**, 433–443.

ROBINSON, S. K. 1991 Coherent motions in the turbulent boundary layer. *Ann. Rev. Fluid Mech.* **23**, 601–639.

SIROVICH, L., KIRBY, M. & WINTER, M. 1990 An eigenfunction approach to large scale transitional structures in jet flow. *Phys. Fluids* A **2**, 127–135.

STONE, E. 1989 A study of low-dimensional models for the wall region of a turbulent boundary layer. PhD thesis, Cornell University.

SWEARINGEN, J. D. & BLACKWELDER, R. F. 1987 The growth and breakdown of streamwise vortices in the presence of a wall. *J. Fluid Mech.* **182**, 255–290.

TORNIAINEN, E. D., HINZ, A. & GOULDIN, F. C. 1997 Tomographic analysis of unsteady, reacting flows. *AIAA Paper* 97-0257.

WALEFFE, F. 1995 Hydrodynamic stability and turbulence: Beyond transients to a self-sustaining process. *Stud. Appl. Maths* **95**, 319–343.

WEBBER, G. A., HANDLER, R. A. & SIROVICH, L. 1997 The karhunen-loeve decomposition of minimal channel flow. *Phys. Fluids* **9**, 1054–1066.

ZHOU, X. & SIROVICH, L. 1992 Coherence and chaos in a model of turbulent boundary layer. *Phys. Fluids* A **12**, 2855–2874.